Bounds and estimates for the effective yield surface of porous media with a uniform or a nonuniform distribution of voids

Nicolas Bilger, François Auslender, Michel Bornert, Hervé Moulinec, André Zaoui

Bounds and estimates for the effective yield surface of porous media with a uniform or a nonuniform distribution of voids

Nicolas Bilger [a,c,d,1], François Auslender [a,b,*], Michel Bornert [a], Hervé Moulinec [c], André Zaoui [a]

[a] *Laboratoire de Mécanique des Solides, École Polytechnique, CNRS, 91128 Palaiseau Cedex, France*
[b] *Laboratoire de Mécanique et d'Ingénieries, Université Blaise Pascal/IFMA, BP 265, 63175 Aubière, France*
[c] *Laboratoire de Mécanique et d'Acoustique, CNRS, 13402 Marseille Cedex 20, France*
[d] *Électricité de France, Site des Renardières, Route de Sens, Écuelles, 77818 Moret sur Loing, France*

This paper aims at studying the effects of a nonuniform distribution of voids on the macroscopic yield response of porous media with a rigid-perfectly plastic matrix. For this purpose, a semi-analytical model, recently proposed by Bilger et al. [Bilger, N., Auslender, F., Bornert, M., Masson, R., 2002. New bounds and estimates for porous media with rigid perfectly plastic matrix. C. R. Mecanique 330, 127–132], is extended to more general situations where the local porosity can fluctuate. The microstructure is described by a generalized Hashin-type assemblage of hollow spheres and the distribution of the local porosity is obtained from a three-dimensional simulated microstructure. The matrix layer around the voids is discretized into concentric sub-layers so as to take better into account the plasticity gradient along the radial direction. Classical homogenization techniques then provide new self-consistent estimates and upper bounds for the macroscopic yield surface. These results are compared first to the predictions of the Gurson model and its extensions and then to numerical results derived from three-dimensional Fast Fourier Transform (FFT) calculations carried out with the same material porosity distribution. A good agreement is obtained with the three-dimensional FFT calculations and with Gurson–Tvergaard's predictions even for high triaxiality and without fitting any parameter. Nevertheless, when the heterogeneous distribution of voids tends to form clusters, the proposed model fails to capture the properties of the macroscopic yield surface for large triaxiality factors.

Keywords: Porous media; Rigid-plastic behavior; Modified secant approach; Morphologically representative patterns; FFT calculations

1. Introduction

Since the pioneer prediction by Gurson (1977) of the macroscopic yield surface of porous media with a rigid-perfectly plastic matrix and spherical voids, a number of contributions have led to significant advances in this field.

* Corresponding author.
E-mail addresses: nicolas.bilger@e-xstream.com (N. Bilger), auslende@lms.polytechnique.fr (F. Auslender), bornert@lms.polytechnique.fr (M. Bornert), moulinec@lma.cnrs-mrs.fr (H. Moulinec), zaoui@lms.polytechnique.fr (A. Zaoui).
[1] Presently at: e-Xstream engineering (L), Ecostart, Rue de l'industrie, L-3895 Foetz, Luxembourg.

First, Gurson's criterion (Eq. (42) in Appendix A) has been shown to yield an upper bound (Perrin, 1992) for microstructures described by a Hashin Composite Sphere Assemblage (CSA, Hashin, 1962). Several modifications have then been proposed to account better for the interactions between voids: Tvergaard (1981) introduced new parameters in the original Gurson criterion (Eq. (43)) from a fitting with numerical simulations carried out on periodic media with an elastic-plastic matrix, which show some strain localization between the voids; Perrin and Leblond (1990) performed an analytical derivation of these parameters from a self-consistent treatment of spherical voids embedded in a matrix satisfying the Gurson–Tvergaard criterion and subjected to a hydrostatic load; in order to capture the acceleration of the cavity growth near coalescence, Tvergaard and Needleman (1984) replaced the actual porosity by an effective larger one. A detailed review of these results can be found, e.g., in Tvergaard (1990).

New advances have been achieved from the application of recent nonlinear homogenization techniques to porous media. The classical linear Hashin–Shtrikman upper bound has been extended to such materials with an isotropic distribution of voids by Ponte Castañeda (1991), Willis (1991) and Michel and Suquet (1992), using three different methods. The obtained upper bound referred to in the sequel as the Hashin–Shtrikman nonlinear bound (Eq. (44)), improves on Gurson's criterion at low triaxiality but yields stiffer predictions for large triaxiality factors. Later on, Gărăjeu and Suquet (1997) proposed a new micromechanical treatment, based on the use of an improved trial velocity field in the hollow sphere with respect to Gurson's one, and they obtained an analytical expression (Eq. (45)) of the macroscopic yield surface which is a rigorous upper bound for microstructures described by a Hashin CSA. It does however not improve on the Hashin–Shtrikman bound for pure shear. That is why a slight modification of their expression (Eq. (47)) has also been proposed as an improved estimate, referred to as Gurson-HS estimate in the sequel, since it fits well with Hashin–Shtrikman's bound for low triaxiality factors and with Gurson's criterion for a hydrostatic loading. Extensions of the Hashin–Shtrikman upper bound to anisotropic viscous porous media, taking into account pore shape, orientation and anisotropy of the pore spatial distribution have also been proposed by Kailasam et al. (1997). They are based on the combination of a general variational principle for nonlinear composites, due to Ponte Castañeda (1992) and based on the use of a Linear Comparison Composite (LCC), with linear Hashin–Shtrikman-type estimates for porous media, such as those proposed by Ponte Castañeda and Willis (1995).

Recent developments have been concerned with efforts to take better into account the actual randomness of the distribution of voids, which in practice differs from a periodic distribution or a Hashin assemblage of hollow spheres with identical porosity. Numerical simulations based on the fast Fourier transform (FFT) technique, initially developed by Moulinec and Suquet (1994) and extended to materials with high contrast between the phases by Michel et al. (2000), have been carried out on porous materials in order to study the influence of the microstructure on the local mechanical responses. From 2D- and 3D-FFT computations performed on virtual many-pores unit-cells exhibiting different void clustering configurations, Bilger et al. (2005) showed that microstructures with connected clusters lead to the softest yield response while random microstructures yield the stiffest one and microstructures with disconnected clusters an intermediate response. Nevertheless, all these responses are softer than those predicted by the Gurson criterion. Moreover, at the local level, numerical simulations revealed a tendency to strain localization into bands between neighbor voids. The gathering of these bands then generates a preferred deformation path throughout the representative volume element (RVE), as also mentioned by Pijnenburg and Van der Giessen (2001) for polymers. However, the determination of the macroscopic response of materials with complex microstructures requires large and expensive computations and the need still exists for simplified models able to restitute the macroscopic behavior in more general morphological situations than those considered by models based on the CSA with uniform porosity, on classical Hashin–Shtrikman bounds or on periodic one-pore unit-cell computations. This question has been recently addressed by Suquet (2005), which provides analytical estimates for the effect of small fluctuations of the volume fraction of constituents on the effective properties of composites. It is also the main goal of the present paper which proposes a nonlinear homogenization treatment relying on the so-called "morphologically representative pattern" (MRP) approach.

This approach initially proposed by Stolz and Zaoui (1991) in the framework of linear homogenization, combines a deterministic description of individual heterogeneous micro-domains, the "representative patterns", and a statistical representation of the spatial distribution of these patterns. It can then deal more precisely with a nonuniform distribution of voids than the classical "point approach", which deals with mechanical phases as a whole, so that sharper bounds and more efficient estimates for the overall properties can be derived. Both generalized linear Hashin–Shtrikman bounds (Stolz and Zaoui, 1991; Bornert et al., 1996) and generalized self-consistent estimates (Bornert, 1996a) can be constructed this way. This approach has especially been applied by Bornert et al. (1994) to a Hashin

assemblage made of arbitrary multi-layered composite spherical pattern, instead of homothetic two-phase composite spheres. In addition, nonlinear constitutive phases have been dealt with by means of the classical secant procedure (Berveiller and Zaoui, 1979) combined with the choice of a nonuniform distribution of secant moduli, which allows to account for the radial gradient of plastic deformation in the pattern, without the cost of large numerical computations. Self-consistent estimates of both the effective behavior and local strain distribution in two-phase almost incompressible elastoplastic materials could be generated this way.

In this paper, a modification of this approach making use of the variational procedure due to Ponte Castañeda (1992), which can be interpreted as a modified secant procedure (Suquet, 1995), is proposed in order to predict the macroscopic yield surface of isotropic porous media with a nonuniform distribution of voids. The present treatment makes again use of a "generalized Hashin multilayer CSA" in order to incorporate both the porosity fluctuations and the gradient of the local plastic flow near the pores. While for quasi-incompressible constituents the discrepancy between the classical and modified secant procedures is limited (Bornert, 1996b), the recourse to the modified secant procedure is here essential in order to describe appropriately the plastic flow under pure hydrostatic load, for which the classical secant approach would predict a rigid response. It can also be used to generate improved rigorous upper bounds of the yield surface, in addition to the self-consistent estimates derived by Bornert et al. (1994).

In Section 2, the foundations of the micromechanical model are presented for both the nonlinear homogenization treatment and the aspects relative to the morphological description of the microstructure. This model is used in Section 3 for the determination of the macroscopic yield surface of a porous body: new self-consistent estimates and upper bounds of the Voigt and Hashin–Shtrikman type for the macroscopic yield surface are derived. In Section 4, these results are compared with those obtained by three-dimensional full-field FFT simulations.

2. Foundations of the proposed model

2.1. Nonlinear homogenization

2.1.1. Local and effective properties

Materials considered here are made of a rigid perfectly plastic matrix containing spherical pores. The matrix is supposed to obey the von Mises criterion with flow stress $\sigma_0 = \sigma_0^m > 0$ and its behavior is characterized equivalently by its strength domain P^m, its stress potential u^m or its dissipation potential w^m, which is the Legendre transform of u^m and coincides with the support function of P^m. They are defined by

$$P^m = \left\{\boldsymbol{\sigma} \mid \sigma_{\text{eq}} \leqslant \sigma_0^m\right\}, \qquad u^m(\boldsymbol{\sigma}) = \begin{cases} 0 & \text{if } \boldsymbol{\sigma} \in P^m, \\ +\infty & \text{otherwise,} \end{cases} \tag{1}$$

$$w^m(\boldsymbol{\varepsilon}) = \sup_{\boldsymbol{\sigma}} \left\{\boldsymbol{\sigma} : \boldsymbol{\varepsilon} - u^m(\boldsymbol{\sigma})\right\} = \sup_{\boldsymbol{\sigma} \in P^m} \{\boldsymbol{\sigma} : \boldsymbol{\varepsilon}\} = \begin{cases} \sigma_0^m \varepsilon_{\text{eq}} & \text{if } \varepsilon_m = 0, \\ +\infty & \text{otherwise,} \end{cases} \tag{2}$$

where $3\varepsilon_m = \text{tr}(\boldsymbol{\varepsilon}) = \boldsymbol{i} : \boldsymbol{\varepsilon}$ is the mean strain rate, $\boldsymbol{i}$ being the second-order identity tensor ($i_{ij} = \delta_{ij}$, with $\boldsymbol{\delta}$ the Kronecker's symbol), $\text{tr}(\boldsymbol{a})$ the trace of tensor $\boldsymbol{a}$ and $\boldsymbol{a} : \boldsymbol{b} = a_{ij} b_{ij}$. The von Mises equivalent stress is as usually defined by $\sigma_{\text{eq}} = \sqrt{\frac{3}{2}\boldsymbol{\sigma} : \boldsymbol{K} : \boldsymbol{\sigma}}$, with $\boldsymbol{K} = \boldsymbol{I} - \boldsymbol{J}$ and $\boldsymbol{J} = \frac{1}{3}\boldsymbol{i} \otimes \boldsymbol{i}$, $\boldsymbol{I}$ being the fourth order identity tensor. The equivalent strain rate is given by $\varepsilon_{\text{eq}} = \sqrt{\frac{2}{3}\boldsymbol{\varepsilon} : \boldsymbol{K} : \boldsymbol{\varepsilon}}$. The fourth-order tensors $\boldsymbol{K}$ and $\boldsymbol{J}$ are the usual projectors on the subspaces of purely deviatoric and spherical second-order tensors, respectively. The strength domain of the pores P^p is restricted to the origin ($\sigma_0^p = 0$), so that their dissipation potential w^p does identically vanish.

The effective strength domain of the porous material occupying the representative volume element V with boundary ∂V is given (Suquet, 1983; Salençon, 1983) by

$$P^{\text{eff}} = \left\{\boldsymbol{\Sigma} \mid \exists \boldsymbol{\sigma},\ \boldsymbol{\sigma} \in S(\boldsymbol{\Sigma}) \text{ and } \boldsymbol{\sigma}(\boldsymbol{x}) \in P(\boldsymbol{x}) \forall \boldsymbol{x} \in V\right\}, \tag{3}$$

where $P(\boldsymbol{x})$ is the local strength domain at point $\boldsymbol{x} \in V$, equal to P^m in the matrix and P^p in the pores, and $S(\boldsymbol{\Sigma})$ is the set of statically admissible stress fields on V balancing the overall stress $\boldsymbol{\Sigma}$

$$S(\boldsymbol{\Sigma}) = \left\{\boldsymbol{\tau}, \text{div}(\boldsymbol{\tau}) = 0 \text{ in } V, \langle\boldsymbol{\tau}\rangle = \boldsymbol{\Sigma}\right\}, \tag{4}$$

where $\langle\cdot\rangle$ denotes the spatial average over V. Note that the details of the boundary conditions applied at the boundary ∂V do not need to be specified, since the overall properties are independent of these, when macrohomogeneity is assumed. Alternatively, the effective strength domain is also given by its support function

$$W(\boldsymbol{E}) = \sup_{\boldsymbol{\Sigma}\in P^{\text{eff}}} \boldsymbol{\Sigma} : \boldsymbol{E}, \tag{5}$$

which obeys the variational formulation

$$W(\boldsymbol{E}) = \inf_{\boldsymbol{v}\in K(\mathbf{E})} \big\langle w\big(\cdot, \boldsymbol{\varepsilon}\big(\boldsymbol{v}(\cdot)\big)\big)\big\rangle, \tag{6}$$

where $w(\boldsymbol{x},\cdot) = \sum_{r=m,p} w^r(\cdot)\kappa^r(\boldsymbol{x})$, with κ^r the characteristic function of phase r, equal to 1 in phase r and zero elsewhere. The set $K(\boldsymbol{E})$ is the set of velocity fields $\boldsymbol{v}$ compatible with the overall strain rate $\boldsymbol{E}$, i.e., such that $\boldsymbol{E} = \int_{\partial V}(\boldsymbol{v}\otimes\boldsymbol{n} + \boldsymbol{n}\otimes\boldsymbol{v})/(2|V|)\,\mathrm{d}s$, where $|V|$ is the measure of V, and $\boldsymbol{n}$ the unit outward normal to ∂V. Note that these velocity fields may exhibit discontinuous tangential component on internal surfaces of V, in which case the integral of ω over V has to be understood in a generalized sense and involves contributions of these discontinuities. In the following, only continuous fields will be used, so that such technical considerations do not need to be developed further. The effective stress associated with a given nonzero macroscopic strain rate is obtained by differentiation of $W(\boldsymbol{E})$ with respect to $\boldsymbol{E}$; it provides a point on the effective yield surface. When an upper bound is available for $W(\boldsymbol{E})$, its differentiation generates an upper bound for the effective yield surface.

Simple bounds of P^{eff} are obtained when uniform stress $\boldsymbol{\sigma}$ or strain rates $\boldsymbol{\varepsilon}$ are considered in Eqs. (3) and (6), respectively. The only admissible homogeneous stress fields are such that $\boldsymbol{\Sigma}\in P(\boldsymbol{x})$, $\forall \boldsymbol{x}\in V$, *i.e.*, such that $\Sigma_{\text{eq}} \leqslant \min_{r=m,p}\sigma_0^r$, which vanishes identically when pores are present in the RVE, whatever their volume fraction. This proves only that P^{eff} contains the origin. On the other hand, the application of Eq. (6) with a homogeneous strain field leads to the inequality

$$W(\boldsymbol{E}) \leqslant \big\langle w(\cdot,\boldsymbol{E})\big\rangle = \begin{cases} \langle\sigma_0^y\rangle E_{\text{eq}} & \text{if } \boldsymbol{i} : \boldsymbol{E} = 0, \\ +\infty & \text{otherwise,} \end{cases}$$

where the field σ_0^y is equal to σ_0^r in phase r. This ensures that the effective strength domain is contained in the domain associated with a von Mises rigid plastic material with a flow stress equal to $(1-f)\sigma_0$, where f is the porosity.

These bounds, which are the extensions of the classical Voigt–Reuss bounds for linear elasticity to rigid perfectly plastic behaviors, incorporate very limited microstructural information on the RVE. In order to derive sharper bounds or better estimates for the macroscopic yield stress, some information must be known and taken into account on the distribution of the constituents inside the RVE, in addition to the mechanical properties of the phases and their volume fractions.

2.1.2. Modified secant approach

The derivation of such more efficient bounds or estimates requires more sophisticated trial fields in the variational formulation (6). A systematic way to generate such fields is to linearize the nonlinear constitutive relations of the phases of the nonlinear composite, in order to be left with a linear homogenization problem on a composite with a similar microstructure and for which efficient homogenization results might be at hand. Various linearization procedures to define this so-called linear comparison composite (LCC, Ponte Castañeda, 1992) have been proposed, including the classical secant linearization (Berveiller and Zaoui, 1979) and its recent modification (Ponte Castañeda, 1992; Suquet, 1995), the tangent linearization (Hill, 1965; Hutchinson, 1970; Molinari et al., 1987; Ponte Castañeda, 1996; Masson et al., 2000, ...) or more elaborate treatments (e.g., Ponte Castañeda, 2002). In the present study, use is made of the variational procedure of Ponte Castañeda (1992) which presents the advantage of generating a LCC with isotropic constituents which can be dealt with analytically in the framework of the pattern-based approach. In addition, when an upper bound is available for the linear effective properties of the LCC, it generates a corresponding upper bound for the effective nonlinear properties, i.e., in the present case, an upper bound for the effective strength domain. It is briefly recalled in what follows in the context of perfect plasticity.

The nonlinear dissipation potential (Eq. (2)) of the matrix is first compared to the potential w_l of a linearly viscous incompressible isotropic material, with arbitrary modulus $\mu > 0$ given by

$$w_l(\mu,\boldsymbol{\varepsilon}) = \begin{cases} \mu\boldsymbol{\varepsilon} : \boldsymbol{K} : \boldsymbol{\varepsilon} = \frac{3}{2}\mu\varepsilon_{\text{eq}}^2 & \text{if } \operatorname{tr}(\boldsymbol{\varepsilon}) = 0, \\ +\infty & \text{otherwise.} \end{cases} \tag{7}$$

From the following inequality which holds true for all trace free strain rate $\boldsymbol{\varepsilon}$ and all positive modulus μ

$$w^m(\boldsymbol{\varepsilon}) = w_l(\mu, \boldsymbol{\varepsilon}) + \big(w^m(\boldsymbol{\varepsilon}) - w_l(\mu, \boldsymbol{\varepsilon})\big) \tag{8}$$

$$\leqslant w_l(\mu, \boldsymbol{\varepsilon}) + \sup_{\boldsymbol{\varepsilon}}\big(w^m(\boldsymbol{\varepsilon}) - w_l(\mu, \boldsymbol{\varepsilon})\big) = w_l(\mu, \boldsymbol{\varepsilon}) + \frac{(\sigma_0^m)^2}{6\mu} \tag{9}$$

and from the identity of w^m and w_l for non-trace free strain rates, the variational relation (Eq. (6)) leads to

$$W(\boldsymbol{E}) \leqslant W_l(\boldsymbol{E}) + \left\langle \frac{(\sigma_0^m)^2}{6\mu(\cdot)} \right\rangle \qquad \text{with } W_l(\boldsymbol{E}) = \inf_{\boldsymbol{v}\in K(\mathbf{E})} \big\langle w_l\big(\mu(\cdot), \boldsymbol{\varepsilon}(\boldsymbol{v})\big)\big\rangle, \tag{10}$$

where the integrations are restricted to the matrix phase since the integrands vanish identically on the pores. Note that the moduli $\mu(\boldsymbol{x})$ of the comparison material may not be constant in the matrix. The first infimum problem consists in finding the effective linear potential of a composite made of an isotropic incompressible matrix with a heterogeneous distribution of moduli $\mu(\boldsymbol{x})$, and the same pore distribution as the initial nonlinear porous medium.

While this problem does not have a simple solution for a general distribution of moduli $\mu(\boldsymbol{x})$, estimates or upper bounds for $W_l(\boldsymbol{E})$ can be obtained in more specific situations, and in particular when $\mu(\boldsymbol{x})$ is piecewise constant. Let Ω_s, $s \in [1, S]$, denote subdomains of the matrix phase on which μ is constant, equal to, say, μ_s when $\boldsymbol{x} \in \Omega_s$ and let $W_l(\mu_1, \ldots, \mu_S, \boldsymbol{E}) = \frac{1}{2}\boldsymbol{E} : \boldsymbol{L}^{\text{eff}}(\mu_1, \ldots, \mu_S) : \boldsymbol{E}$ be an upper bound of $W_l(\boldsymbol{E})$ in this case. The best upper bound is obtained when the right-hand side of Eq. (10) is optimized with respect to the choice of the μ_s, that is when the moduli satisfy

$$\forall s \in [1, S] \quad \boldsymbol{E} : \frac{\partial \boldsymbol{L}^{\text{eff}}}{\partial \mu_s}(\mu_1, \ldots, \mu_S) : \boldsymbol{E} = f_s \frac{\sigma_0^2}{3\mu_s^2}, \tag{11}$$

where f_s is the volume fraction of domain Ω_s in V. The left-hand side of this equality is proportional to the second-order moment of the local equivalent strain on subdomain Ω_s in the considered $(S + 1)$ phase linear comparison composite submitted to the overall strain rate $\boldsymbol{E}$, as established by Kreher (1990)

$$\frac{2}{3}\boldsymbol{K} :: \langle \boldsymbol{\varepsilon} \otimes \boldsymbol{\varepsilon} \rangle_s = \big\langle \varepsilon_{\text{eq}}^2 \big\rangle_s = \frac{1}{3 f_s}\boldsymbol{E} : \frac{\partial \boldsymbol{L}^{\text{eff}}}{\partial \mu_s}(\mu_1, \ldots, \mu_S) : \boldsymbol{E}. \tag{12}$$

It follows that the optimal moduli of the subdomains Ω_s are the secant moduli of the matrix associated with the second-order moment in these subdomains of the strain rate in the LCC submitted to the overall rate $\boldsymbol{E}$, as pointed out by Suquet (1995)

$$\mu_s = \frac{\sigma_0}{3\sqrt{\langle \varepsilon_{\text{eq}}^2 \rangle_s}}. \tag{13}$$

In the following derivations, the spatial distribution of the domains Ω_s will be such that $\boldsymbol{L}^{\text{eff}}$ is isotropic and reads $\boldsymbol{L}^{\text{eff}} = 3k^{\text{eff}}\boldsymbol{J} + 2\mu^{\text{eff}}\boldsymbol{K}$, where k^{eff} is not infinite because of the presence of the pores, even if the subphases in the matrix are incompressible. The overall dissipation potential of the porous medium is then bounded by

$$W(\boldsymbol{E}) \leqslant W_{\text{var}}(\boldsymbol{E}) = \frac{9}{2}k^{\text{eff}}(\mu_1, \ldots, \mu_S)E_m^2 + \frac{3}{2}\mu^{\text{eff}}(\mu_1, \ldots, \mu_S)E_{\text{eq}}^2 + \frac{\sigma_0^2}{6}\sum_{s=1}^{S}\frac{f_s}{\mu_s^2} \tag{14}$$

$$\text{with } \forall s \in [1, S] \quad \mu_s = \frac{\sigma_0}{3\sqrt{\langle \varepsilon_{\text{eq}}^2 \rangle_s}} \quad \text{and} \quad f_s\big\langle \varepsilon_{\text{eq}}^2 \big\rangle_s = 3\frac{\partial k^{\text{eff}}}{\partial \mu_s}E_m^2 + \frac{\partial \mu^{\text{eff}}}{\partial \mu_s}E_{\text{eq}}^2. \tag{15}$$

Since the secant moduli μ_s are optimal, the derivative of $W_{\text{var}}(\boldsymbol{E})$ with respect to $\boldsymbol{E}$ can be obtained from the partial derivative of the right-hand side of Eq. (14) with respect to $\boldsymbol{E}$ only, assuming the μ_s constant. As a consequence, the obtained overall stress coincides with the macroscopic stress in the LCC, and reads

$$\boldsymbol{\Sigma} = \big[3k^{\text{eff}}(\mu_1, \ldots, \mu_S)\boldsymbol{J} + 2\mu^{\text{eff}}(\mu_1, \ldots, \mu_S)\boldsymbol{K}\big] : \boldsymbol{E}. \tag{16}$$

From previous expressions (Eqs. (14) and (15)), it is clear that $W_{\text{var}}(\boldsymbol{E})$ is a function of the two first invariants of $\boldsymbol{E}$ only, E_m and E_{eq}, which ensures that the obtained upper bound on the strength domain is totally determined in the

$(\Sigma_m, \Sigma_{\rm eq})$ plane. This is a direct consequence of the assumed isotropy of the spatial distribution of the secant moduli. To construct this boundary, it is convenient to determine the yield strength at fixed macroscopic stress triaxiality ratio $\tau = \Sigma_m/\Sigma_{\rm eq}$. This is obtained when the relation $k^{\rm eff}E_m = \tau\mu^{\rm eff}E_{\rm eq}$ is enforced, so that second-order moment are computed as

$$\left\langle \varepsilon_{\rm eq}^2 \right\rangle_s = \frac{1}{f_s}\left(3\left[\tau\frac{\mu^{\rm eff}}{k^{\rm eff}}\right]^2\frac{\partial k^{\rm eff}}{\partial \mu_r} + \frac{\partial \mu^{\rm eff}}{\partial \mu_r}\right)E_{\rm eq}^2. \tag{17}$$

For a given triaxiality ratio and a fixed overall equivalent strain rate, the S secant moduli μ_s and the S second-order moments $\langle\varepsilon_{\rm eq}^2\rangle_s$ are solutions of the nonlinear system of Eqs. (17) and (13), which can for instance be solved by a fixed-point algorithm initialized with $\langle\varepsilon_{\rm eq}^2\rangle_s = E_{\rm eq}^2$. Once convergence is reached, the point $(\Sigma_m = \tau\Sigma_{\rm eq}, \Sigma_{\rm eq} = 3\mu^{\rm eff}(\mu_1, \ldots, \mu_S)E_{\rm eq}^2)$ lies on the wanted yield surface.

The functions $\mu^{\rm eff}$ and $k^{\rm eff}$ are provided by an adequate linear homogenization model, appropriate for the microstructure of the considered LCC with $(S+1)$ phases. When these functions provide estimates or lower bounds of its effective linear properties instead of upper bounds, the obtained yield surface is an estimate of the effective yield surface of the nonlinear porous material.

When $S = 1$ and when the pore distribution is isotropic, the linear Hashin–Shtrikman upper bound (Hashin and Shtrikman, 1963) can be used. One can show that the obtained macroscopic yield surface corresponds to the so-called nonlinear Hashin–Shtrikman bound (Eq. (44) in Appendix A). As already mentioned in Section 1, this bound is above the Gurson bound for high triaxiality ratios. This is due to the use of uniform secant moduli in the matrix, whereas the actual secant moduli strongly fluctuate between neighboring voids (Bilger et al., 2005). Better bounds are likely to be obtained with a refined description of both the heterogeneity of the secant moduli in the matrix and the heterogeneous distribution of voids in the RVE. Some progress in this direction is expected from the use of the MRP approach, as proposed in the next section.

2.2. Morphological description

Besides the choice of a nonlinear homogenization method, one has to specify the way the actual morphology of the concerned material is taken into account. For a two-phase porous material, the details of the spatial distribution of voids cannot be accounted for by use of the classical "point approach" where the different phases are considered as a whole so that fluctuations of the local porosity cannot be described. The so-called "pattern approach", which is adopted by the MRP theory, offers a more appropriate framework for an improved description of the void distribution. It is first briefly recalled before specialization to the problem under investigation.

2.2.1. The morphologically representative pattern approach

The MRP approach (Stolz and Zaoui, 1991) is concerned with heterogeneous media which can be decomposed into a set of "patterns", which are families of identical finite composite domains whose material content is known. In each pattern λ, one can consider "homologous points", e.g., the pattern centers $\boldsymbol{X}_\lambda^k$, which have the same relative location in the N_λ different domains D_λ^k. For an elastic material with the elastic moduli $\boldsymbol{C}(\boldsymbol{x})$, this means that, if $\boldsymbol{y} = \boldsymbol{X}_\lambda^k + \boldsymbol{x} \in D_\lambda^k$, then $\boldsymbol{y}' = \boldsymbol{y} + \boldsymbol{X}_\lambda^l - \boldsymbol{X}_\lambda^k = \boldsymbol{X}_\lambda^l + \boldsymbol{x} \in D_\lambda^l$ and $\boldsymbol{C}(\boldsymbol{y}) = \boldsymbol{C}(\boldsymbol{y}')$, i.e., $\boldsymbol{C}(\boldsymbol{X}_\lambda^k + \boldsymbol{x}) = \boldsymbol{C}(\boldsymbol{X}_\lambda^l + \boldsymbol{x})$. A pattern λ is defined (see Fig. 1) by one domain centered at the origin, say D_λ, with volume V_λ, by the spatial distribution of the local moduli within this domain, $\boldsymbol{C}_\lambda(\boldsymbol{x})$, $\forall \boldsymbol{x} \in D_\lambda$, by the volume fraction c_λ of the union of its domains within the RVE and by the positions $\boldsymbol{X}_\lambda^k$ of the centers of the patterns in the RVE. The heterogeneous material is completely characterized by the description of all its patterns and by the spatial distribution of the centers $\boldsymbol{X}_\lambda^k$, $\forall k \in [1, N_\lambda]$, $\forall \lambda \in [1, P]$, P being the number of pattern.

When the union of all domains of all patterns fills the whole RVE, the microstructure of the latter is totally determined, and can be referred to as a generalized Hashin's assemblage of patterns. This is however not necessarily the case (Bornert, 2001). When the patterns do not fill completely the RVE, one may assume that the surrounding domain D_0 is occupied by a single homogeneous phase, with volume fraction c_0 and moduli $\boldsymbol{C}_0 = \boldsymbol{S}_0^{-1}$, which can – but does not need to – be described by an additional homogeneous pattern.

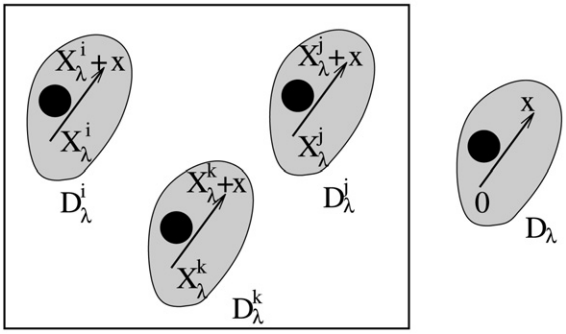

Fig. 1. A morphologically representative pattern.

For homogeneous boundary conditions on the RVE V, generalized Voigt–Reuss type bounds can be easily derived by transferring these conditions on the boundary of each domain D_λ^k, namely

$$\boldsymbol{u}'_\lambda(\boldsymbol{x}) = \boldsymbol{E}\cdot\boldsymbol{x}, \quad \text{or} \quad \boldsymbol{\sigma}'_\lambda(\boldsymbol{x})\cdot\boldsymbol{n}_\lambda(\boldsymbol{x}) = \boldsymbol{\Sigma}\cdot\boldsymbol{n}_\lambda(\boldsymbol{x}), \quad \boldsymbol{x}\in\partial D_\lambda^k,\ \forall k\in[1,N_\lambda],\ \forall\lambda\in[1,P], \tag{18}$$

where $\boldsymbol{u}'_\lambda(\boldsymbol{x})$ and $\boldsymbol{\sigma}'_\lambda(\boldsymbol{x})$ are kinematically and statically admissible trial fields, respectively, and $\boldsymbol{n}_\lambda$ the unit outward normal vector to ∂D_λ. In the surrounding matrix, classical homogeneous trial strain and stress fields are used: $\boldsymbol{u}'_\lambda(\boldsymbol{x}) = \boldsymbol{E}\cdot\boldsymbol{x}$ and $\boldsymbol{\sigma}'(\boldsymbol{x}) = \boldsymbol{\Sigma}$ for $\boldsymbol{x}\in D_0$. From the (either analytical or numerical) computation of the corresponding solutions $\boldsymbol{\varepsilon}'_\lambda(\boldsymbol{x})$ and $\boldsymbol{\sigma}'_\lambda(\boldsymbol{x})$ in $D_\lambda, \forall\lambda$, the Voigt-type bound for the moduli $\boldsymbol{C}^V_{\mathrm{MRP}}$ reads

$$\boldsymbol{C}^V_{\mathrm{MRP}} \geqslant \boldsymbol{C}^{\mathrm{eff}}, \qquad \boldsymbol{C}^V_{\mathrm{MRP}} : \boldsymbol{E} = \langle \boldsymbol{C} : \boldsymbol{\varepsilon}'\rangle = c_0\boldsymbol{C}_0 : \boldsymbol{E} + \sum_{\lambda=1}^{P} c_\lambda \langle \boldsymbol{C}_\lambda : \boldsymbol{\varepsilon}'_\lambda\rangle_{D_\lambda} \quad \forall \boldsymbol{E} \tag{19}$$

whereas the Reuss-type bound for the compliances $\boldsymbol{S}^R_{\mathrm{MRP}}$ is

$$\left(\boldsymbol{S}^R_{\mathrm{MRP}}\right)^{-1} \leqslant \boldsymbol{C}^{\mathrm{eff}}, \qquad \boldsymbol{S}^R_{\mathrm{MRP}} : \boldsymbol{\Sigma} = \langle \boldsymbol{S} : \boldsymbol{\sigma}'\rangle = c_0\boldsymbol{S}_0 : \boldsymbol{\Sigma} + \sum_{\lambda=1}^{P} c_\lambda \langle \boldsymbol{S}_\lambda : \boldsymbol{\sigma}'_\lambda\rangle_{D_\lambda} \quad \forall \boldsymbol{\Sigma} \tag{20}$$

with $\boldsymbol{S}_\lambda(\boldsymbol{x})$ the local elastic compliances and $\langle \boldsymbol{a}\rangle_{D_\lambda}$ the average of $\boldsymbol{a}$ over domain D_λ.

In order to derive sharper bounds or estimates for the effective properties of such linear heterogeneous media, Stolz and Zaoui (1991) used the classical variational approach of Hashin and Shtrikman (1963) with nonuniform polarization fields $\boldsymbol{p}^*$ within the domains, taking the same value at homologous points of every pattern λ

$$\boldsymbol{p}^*_\lambda(\boldsymbol{x}) = \boldsymbol{p}^*\left(\boldsymbol{x} + \boldsymbol{X}^k_\lambda\right) \quad \forall \boldsymbol{x}\in D_\lambda,\ \forall k,\ \forall\lambda. \tag{21}$$

A classical homogeneous polarization field $\boldsymbol{p}^*_0$ is used in the matrix outside the patterns. These fields generate strain $\boldsymbol{\varepsilon}^*(\boldsymbol{p}^*)$ and stress fields $\boldsymbol{\sigma}^* = \boldsymbol{C}^0 : \boldsymbol{\varepsilon}^*(\boldsymbol{p}^*) + \boldsymbol{p}^*$ on a fictitious homogeneous reference medium with arbitrary elastic moduli $\boldsymbol{C}^0$ and the same geometry and boundary conditions as the actual RVE, which can be used as admissible trial fields for the initial problem. They are introduced into the Hashin–Shtrikman functional HS^0

$$2HS^0(\boldsymbol{p}^*, \boldsymbol{E}) = \boldsymbol{E} : \boldsymbol{C}^0 : \boldsymbol{E} + \boldsymbol{E} : \langle \boldsymbol{p}^*\rangle + \left\langle \boldsymbol{\varepsilon}^*(\boldsymbol{p}^*) : \boldsymbol{p}^*\right\rangle - \left\langle \boldsymbol{p}^* : (\delta\boldsymbol{C}^0)^{-1} : \boldsymbol{p}^*\right\rangle, \tag{22}$$

which yields upper and lower bounds for the effective linear strain energy $W(\boldsymbol{E})$ of the initial problem for any choice of $\boldsymbol{p}^*$ as soon as the moduli $\boldsymbol{C}^0$ are chosen in an appropriate way: if $\delta\boldsymbol{C}^0 = [\boldsymbol{C}(\boldsymbol{x}) - \boldsymbol{C}^0]$ is negative or positive definite at any point $\boldsymbol{x}\in V$, then HS^0 leads to an upper or a lower bound for $W(\boldsymbol{E})$. Under the assumption of macrohomogeneity, the local stress and strain fields $\boldsymbol{\sigma}^*$ and $\boldsymbol{\varepsilon}^*$ are derived from the use of Green techniques and of the so-called Green strain operator $\boldsymbol{\Gamma}^0(\boldsymbol{x}-\boldsymbol{x}')$ relative to an infinite body with moduli $\boldsymbol{C}^0$ through the equation

$$\boldsymbol{\varepsilon}^*(\boldsymbol{x}) = \boldsymbol{E} - \int_V \boldsymbol{\Gamma}^0(\boldsymbol{x}-\boldsymbol{x}') : \left(\boldsymbol{p}^*(\boldsymbol{x}') - \langle \boldsymbol{p}^*\rangle\right) \mathrm{d}\omega(\boldsymbol{x}') \tag{23}$$

which ensures the average condition $\langle \boldsymbol{\varepsilon}^*\rangle = \boldsymbol{E}$.

Optimal bounds are obtained when the polarization fields are chosen such as to minimize or maximize the functional HS^0. A convenient way to derive explicit bounds relies in the definition of "pattern-based average values", say $f_\lambda^M(\boldsymbol{x})$ for pattern λ, which are associated with any field $f(\boldsymbol{x})$ defined on V through

$$f_\lambda^M(\boldsymbol{x}) = \frac{1}{N_\lambda}\sum_{k=1}^{N_\lambda} f\big(\boldsymbol{x}+\boldsymbol{X}_\lambda^k\big), \quad \forall\lambda. \tag{24}$$

Optimal polarization fields $\boldsymbol{p}$ are such that $\boldsymbol{p}_\lambda(\boldsymbol{x}) = (\boldsymbol{C}_\lambda(\boldsymbol{x}) - \boldsymbol{C}^0) : \boldsymbol{\varepsilon}(\boldsymbol{p})_\lambda^M(\boldsymbol{x}), \forall \boldsymbol{x} \in D_\lambda$, for all patterns λ and $\boldsymbol{p}_0 = (\boldsymbol{C}_0 - \boldsymbol{C}^0) : \langle\boldsymbol{\varepsilon}(\boldsymbol{p})\rangle_0$, where $\langle\boldsymbol{\varepsilon}(\boldsymbol{p})\rangle_0$ is the average of $\boldsymbol{\varepsilon}(\boldsymbol{p})$ in the matrix outside the patterns.

Under the hypothesis of an ellipsoidal distribution of the domain centers, it can be shown (Bornert et al., 1996) that the resulting optimized pattern-based strain averages are the solution of Eshelby-type inhomogeneity problems where the infinite matrix, subjected to a same uniform strain $\boldsymbol{E}^0$ at infinity, has the moduli $\boldsymbol{C}^0$ and the ellipsoidal composite inhomogeneities are the different (ellipsoidal) patterns by turn, the possible surrounding matrix being itself treated as a homogeneous pattern with same shape. The governing equations read as follows (with $\boldsymbol{\varepsilon}_0^M(\boldsymbol{x}) = \langle\boldsymbol{\varepsilon}(\boldsymbol{p})\rangle_0$ for convenience)

$$\forall\lambda \in [0, P],\ \forall \boldsymbol{x} \in D_\lambda, \quad \boldsymbol{\varepsilon}_\lambda^M(\boldsymbol{x}) = \boldsymbol{E}^0 - \int_{D_\lambda} \boldsymbol{\Gamma}^0(\boldsymbol{x}-\boldsymbol{x}')\big(\boldsymbol{C}_\lambda(\boldsymbol{x}') - \boldsymbol{C}^0\big) : \boldsymbol{\varepsilon}_\lambda^M(\boldsymbol{x}')\,\mathrm{d}\omega(\boldsymbol{x}'). \tag{25}$$

The strain rate $\boldsymbol{E}^0$ is determined by the condition $\sum_{\lambda=0}^P c_\lambda \langle\boldsymbol{\varepsilon}_\lambda^M\rangle_{D_\lambda} = \boldsymbol{E}$. Note that for the isotropic distribution of pattern centers considered hereafter, a consistent and in some sense optimal description of the microstructure requires the patterns outer shape D_λ to be all spherical, though is not specifically required when the volume fraction of the surrounding matrix is not zero.

Finally, the generalized Hashin–Shtrikman tensor of elastic moduli $\boldsymbol{C}_{\mathrm{MRP}}^{\mathrm{HS}}$, obtained with reference medium $\boldsymbol{C}^0$, is identified from the relations

$$\forall \boldsymbol{E}, \quad \boldsymbol{C}_{\mathrm{MRP}}^{\mathrm{HS}}\big(\boldsymbol{C}^0\big) : \boldsymbol{E} = \sum_{\lambda=0}^{P} c_\lambda \big\langle \boldsymbol{C}_\lambda : \boldsymbol{\varepsilon}_\lambda^M \big\rangle_{D_\lambda}. \tag{26}$$

It is an upper or a lower bound of the effective tensor of moduli when $\boldsymbol{C}^0$ is chosen as specified above. Alternatively, generalized self-consistent estimates $\boldsymbol{C}_{\mathrm{MRP}}^{\mathrm{SC}}$ are defined as the solutions of the implicit equation $\boldsymbol{C}_{\mathrm{MRP}}^{\mathrm{HS}}(\boldsymbol{C}_{\mathrm{MRP}}^{\mathrm{SC}}) = \boldsymbol{C}_{\mathrm{MRP}}^{\mathrm{SC}}$, which can easily be solved iteratively.

When applied to the classical CSA, where all the composite spheres with the same diameter define one pattern, and under the assumption of an isotropic distribution of the sphere centers, the various resulting Eshelby-type problems are identical and new Hashin–Shtrikman-type bounds are easily derived analytically (Hervé et al., 1991), while the corresponding self-consistent estimates coincide with the three-phase model of Christensen and Lo (1979). For the isotropic generalized CSA, several Eshelby-type problems must be solved either numerically, when the spherical domains content is arbitrary, or analytically for simpler geometries, as shown below. In what follows, for ease of notation, the superscript M used for the definition of the "pattern-based average values" in Eq. (24) will be omitted, unless otherwise specified.

2.2.2. Pattern-based description of porous media

We now assume that the microstructure of the porous medium consists of hollow spheres with different local volume fractions and different outer radii embedded in a homogeneous surrounding matrix which has the same properties as the shell of the hollow spheres. When the volume fraction of the surrounding domain vanishes, the resulting microstructure belongs to the class of generalized Hashin composite spheres assemblages (Bornert et al., 1994, (Fig. 2(b))).

As mentioned above, the spherical shape of the patterns, say the hollow spheres, is consistent with the assumption that the distribution of the pore centers is isotropic, whereas the patterns composition reflects the actual morphology of the pores. For simplicity, we assume the pores to be spherical. The local porosity of each pattern is defined by $f_\lambda = V_\lambda^p / V_\lambda$, where V_λ^p denotes the volume of the pores inside pattern λ. Accordingly, the macroscopic porosity reads

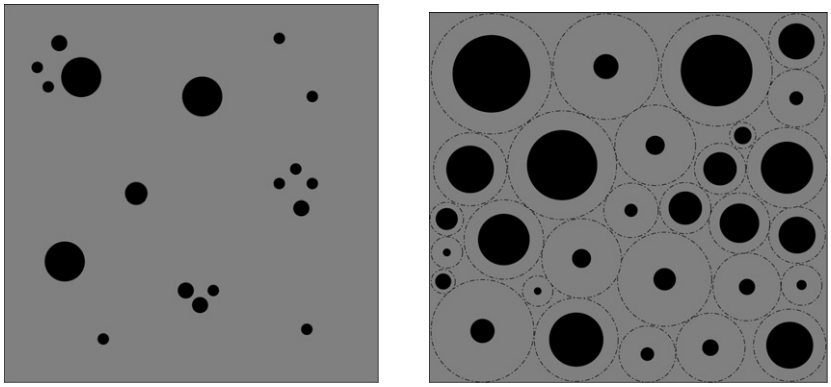

(a) (b)

Fig. 2. (a) Microstructure of a porous medium with a nonuniform distribution of porosity. (b) The isotropic generalized Hashin CSA associated with the microstructure (a).

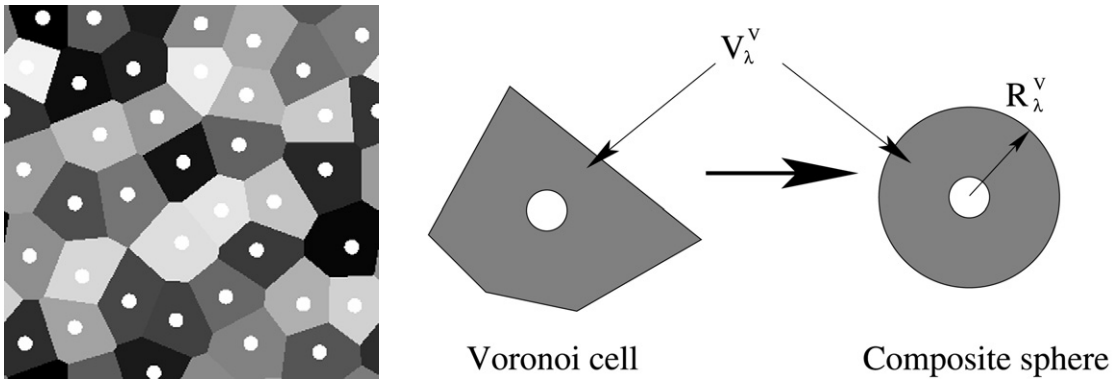

(a) (b)

Fig. 3. (a) Partition of the RVE into Voronoï cells. (b) Rule of the patterns construction: Voronoï cell ≡ Spherical pattern with the same volume.

$$f = \sum_{\lambda=1}^{P} c_\lambda f_\lambda \quad \text{with} \sum_{\lambda=0}^{P} c_\lambda = 1 \text{ and } c_\lambda = \frac{V_\lambda}{|V|}, \ \forall \lambda \in [1, P]. \tag{27}$$

Unlike the classical Hashin CSA which only incorporates the macroscopic porosity, the above description of the microstructure allows us to take the local porosity fluctuations into account.

2.2.3. Porosity distribution

Two different methods are proposed to derive the distribution function of the local porosity of a given porous material. The first, referred to as the "Voronoï model" relies on a partition of the RVE into classical Voronoï cells. The Voronoï cell of a pore is defined as the set of points closer to the center of the considered pore than to all other centers. It is delimited by the bisector planes of the segment connecting the pore center to its neighbors. Such a partition is illustrated in Fig. 3(a) for a two dimensional periodic simulated microstructure. Each Voronoï cell (Fig. 3(b)) can then be represented by a hollow spherical cell of identical volume $V_\lambda^V = \frac{4\pi}{3}(R_\lambda^V)^3$ where R_λ^V denotes the radius of the hollow sphere λ. Accordingly, the local porosity of pattern λ is given by $f_\lambda^V = V_\lambda^p / V_\lambda^V$ whereas the volume fraction of the pattern c_λ^V is given by $c_\lambda^V = V_\lambda^V / V$, while $c_0^V = 0$.

An alternative method consists in defining the patterns from the Stienen model (Coster and Chermant, 2002). This latter also relies on a partition of the RVE into Voronoï cells but it leads to define a hollow sphere (i.e., a pattern) associated with a Voronoï cell as the largest sphere centered on the pore λ and strictly included inside the Voronoï cell (Fig. 4(b)). Accordingly, the radius R_λ^S associated with the pattern λ is easily computed as half the distance between

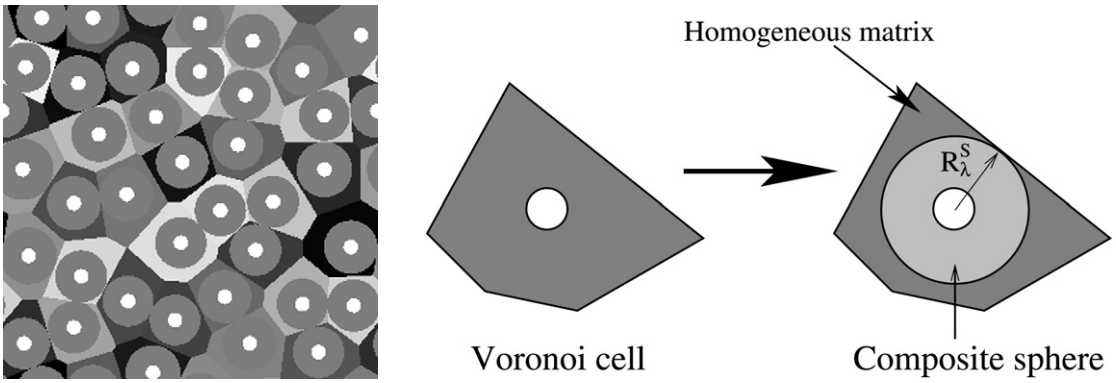

(a) (b)

Fig. 4. (a) Partition of the RVE according to the Stienen model. (b) Rule of the patterns construction: Voronoï cell ≡ composite inclusion + homogeneous matrix.

the center of this pore and the center of its nearest neighbor, while the computation of R_λ^V from the positions of the pore centers requires more sophisticated algorithms. The construction of the Stienen model prevents the patterns to overlap and allows them to come into contact (Fig. 4(a)) in some particular configurations. Again, the local porosity of pattern λ is defined as the ratio between the volume of the pore and that of the hollow sphere, i.e., $f_\lambda^S = V_\lambda^P / V_\lambda^S$ with $V_\lambda^S = \frac{4}{3}\pi (R_\lambda^S)^3$. The concentration of pattern λ is still given by the ratio between the volume of the hollow sphere λ and the volume of the RVE, $c_\lambda^S = V_\lambda^S / |V|$. It is clear that, for the pattern constructed on the same pore λ with both procedures, one has $f_\lambda^S > f_\lambda^V$ and $c_\lambda^S < c_\lambda^V$. As shown in Fig. 4(b), there is in addition some matrix left inside the Voronoï cell once the composite sphere is removed. The volume fraction of all the remaining matrix material over the RVE is given by

$$c_0^S = 1 - \sum_{\lambda=1}^{P} c_\lambda^S > 0. \tag{28}$$

Note that in the above descriptions, each pore defines its own pattern and local volume fraction, generating a discrete distribution function of local porosities. In case of representative volume elements with large numbers of pores, or more generally when statistical averages over a large number of realizations of a same random distribution of pores are considered, continuous distribution functions could easily be generated, for instance by an appropriate smooth interpolation of the cumulative distribution function and its differentiation. In addition, since both construction procedures do not involve any preferred orientation, the obtained pattern description retains the actual statistical symmetry of the initial microstructure, with in particular an isotropic distribution of pattern centers if the pore distribution was originally isotropic.

Let us finally stress out that the definition of the patterns and the local volume fractions according to the Stienen model is fully consistent with the pattern-based description of microstructures, since pattern centers coincide exactly with the actual pore centers and there is no overlapping of the patterns. On the other hand, with the definition of local volume fractions according to the Voronoï model, the actual microstructure is implicitly represented by a generalized composite spheres assemblage, which is another microstructure: for instance, the requirement that the whole RVE be filled with composite spheres requires a fractal construction, which is usually not the case of real porous microstructures. It can however also be pointed out that the Stienen construction is not optimal since many hollow spheres do not touch any neighbor sphere, as seen on Fig. 4(a), so that larger pattern could in principle be used, with which improved bounds and estimates could be obtained. This however requires more sophisticated image analysis procedures, which are left for further investigations.

2.3. Full solution to the nonlinear homogenization problem

The previous pattern description would be sufficient for the investigation of linear properties. However, as pointed out in Section 2.1.2, improved nonlinear bounds are obtained when the matrix is decomposed into subdomains in order

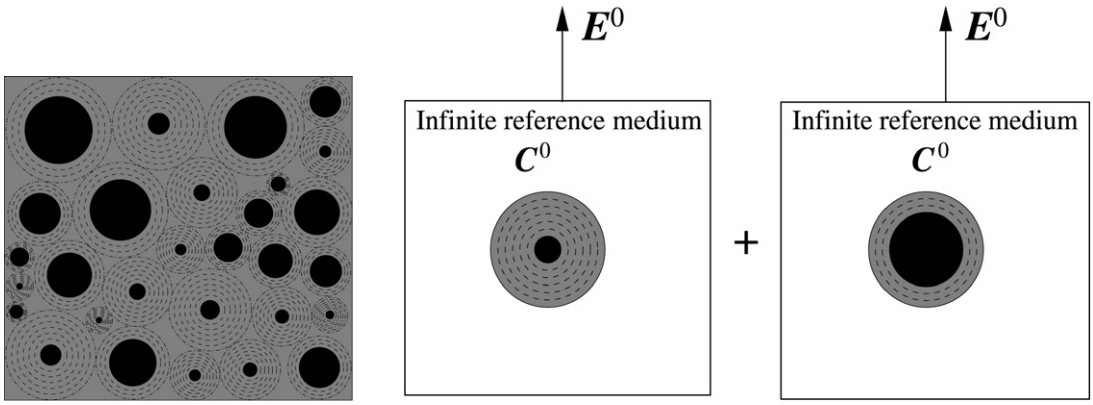

(a) (b)

Fig. 5. (a) Generalized Hashin multilayer CSA (two patterns). (b) Associated multilayer composite inclusion problems.

to better account for local strain rate gradients. In the present model, the matrix in each hollow sphere is discretized into concentric layers (see Fig. 5(a)), each having its own homogeneous secant shear modulus. In the sequel, the L_λ layers in the matrix of the pattern $\lambda \in [1, P]$ are numbered from $i = 2$ for the innermost to $i = L_\lambda + 1$ for the outermost and the secant shear modulus of layer i of pattern λ reads μ_λ^i. The index $i = 1$ refers to the core of the multilayered inclusions, i.e., the pore, with $\mu_\lambda^1 = 0$, for $\lambda \geqslant 1$. The volume fraction of the layer i in the composite inclusion λ is f_λ^i. The additional matrix not included in the patterns has its own shear modulus μ_0.

The choice of concentric subdomains ensures that the solution of the auxiliary problems governed by the general equations (25), now made up of a multilayer composite sphere (the pattern λ) embedded in an infinite linear isotropic medium $\boldsymbol{C}^0 = 3k^0\boldsymbol{J} + 2\mu^0\boldsymbol{K}$ submitted to the homogeneous strain $\boldsymbol{E}^0$ at infinity (Fig. 5(b)), has an analytical solution. This solution, due to Hervé and Zaoui (1993) for compressible isotropic phases, is here slightly modified in order to deal with incompressible layers. For that purpose, the four integration constants (A_i, B_i, C_i, D_i) relative to pure shear (see e.g., Eq. (22) of Hervé and Zaoui, 1993) are in the present implementation replaced by the new set of constants $(A_i, B_i/(1-2\nu_i), C_i, D_i/(1-2\nu_i))$, where ν_i is the Poisson's ratio of layer i, so that the factors $1/(1-2\nu_i)$ disappear in all expressions, suppressing the bad numerical behavior of the initial expressions when ν_i tends to 0.5. Except this minor modification, expressions of Hervé and Zaoui (1993) are used without further change and the incompressibility of the phases is simply obtained by using a compression modulus k_i much larger than the shear modulus (in practice $k_i = 10^{30}$, while secant shear moduli typically range from 1 to 1000). In addition, it can also be checked that:

- expressions of Hervé and Zaoui (1993) apply without special treatment when the core of the composite multilayered inclusion is a pore ($\mu_\lambda^1 = k_\lambda^1 = 0$) as in the present situation. The integration constants in the pore are undetermined but not required;
- when the properties of the infinite reference medium are much stiffer than that of the constitutive phases, the solution is identical to that obtained when the displacement $\boldsymbol{E}^0 \cdot \boldsymbol{x}$ is applied at the boundary of the outermost layer, as required for the computation of the pattern-based Voigt bound (19), without any numerical difficulty;
- similarly, when the properties of the infinite reference medium are much softer (but not null) than that of the constitutive phases, the solution is identical to that obtained with a homogeneous stress vector $\boldsymbol{\Sigma}^0 \cdot \boldsymbol{n} = \boldsymbol{C}^0 : \boldsymbol{E}^0 \cdot \boldsymbol{n}$ applied at the boundary of the outermost layer, as required for the computation of the pattern-based Reuss bound (20), again without difficulty;
- the expressions also hold for the homogeneous inclusion problem relative to the matrix surrounding the patterns, if present. In that case, $L_\lambda = 0$ and the classical Eshelby solution is obviously recovered.

These expressions, not detailed here for conciseness, provide the linear dependence of the average strain and stress in layer i of pattern $\lambda \geqslant 0$ with the strain $\boldsymbol{E}^0$ imposed at infinity, in the following isotropic form, as expected from the isotropy of the linear behavior of the layers and the geometry

$$\boldsymbol{\varepsilon}_\lambda^i = \langle \boldsymbol{\varepsilon}_\lambda \rangle_i = \left[a_\lambda^i\left(\mu_\lambda^1, k_\lambda^1, \mu_\lambda^2, \ldots, k_\lambda^{L_\lambda+1}, \mu^0, k^0\right)\boldsymbol{J} + b_\lambda^i\left(\mu_\lambda^1, k_\lambda^1, \mu_\lambda^2, \ldots, k_\lambda^{L_\lambda+1}, \mu^0, k^0\right)\boldsymbol{K} \right] : \boldsymbol{E}^0, \tag{29}$$

$$\boldsymbol{\sigma}_\lambda^i = \langle \boldsymbol{\sigma}_\lambda \rangle_i = \left[3k_\lambda^i a_\lambda^i\left(\mu_\lambda^1, k_\lambda^1, \mu_\lambda^2, \ldots, k_\lambda^{L_\lambda+1}, \mu^0, k^0\right)\boldsymbol{J} + 2\mu_\lambda^i b_\lambda^i\left(\mu_\lambda^1, k_\lambda^1, \mu_\lambda^2, \ldots, k_\lambda^{L_\lambda+1}, \mu^0, k^0\right)\boldsymbol{K}\right] : \boldsymbol{E}^0, \quad (30)$$

where $\mu_\lambda^1 = k_\lambda^1 = 0$ for $\lambda > 0$, $\mu_0^1 = \mu_0$ and k_0^1 arbitrarily large. The tensor $\boldsymbol{C}_{\mathrm{MRP}}^{\mathrm{HS}}(\boldsymbol{C}^0)$ which is determined by Eq. (26) and reads now $3k_{\mathrm{MRP}}^{\mathrm{HS}}\boldsymbol{J} + 2\mu_{\mathrm{MRP}}^{\mathrm{HS}}\boldsymbol{K}$, is computed according to

$$k_{\mathrm{MRP}}^{\mathrm{HS}} \cdot \sum_{\lambda=0}^{P} c_\lambda \sum_{i=1}^{L_\lambda+1} f_\lambda^i a_\lambda^i = \sum_{\lambda=0}^{P} c_\lambda \sum_{i=1}^{L_\lambda+1} f_\lambda^i k_\lambda^i a_\lambda^i, \quad (31)$$

$$\mu_{\mathrm{MRP}}^{\mathrm{HS}} \cdot \sum_{\lambda=0}^{P} c_\lambda \sum_{i=1}^{L_\lambda+1} f_\lambda^i b_\lambda^i = \sum_{\lambda=0}^{P} c_\lambda \sum_{i=1}^{L_\lambda+1} f_\lambda^i \mu_\lambda^i b_\lambda^i. \quad (32)$$

The contribution of the homogeneous pattern representing the matrix outside the hollow spheres is taken into account through index $\lambda = 0$. In case of a generalized Hashin's assemblage, it vanishes and expressions of Bornert et al. (1994) are recovered. Let us recall that in these expressions the compression moduli k_λ^i of all layers except the cores representing the pores, are chosen arbitrarily large with respect to all secant moduli μ_λ^i, so that the final expression of $k_{\mathrm{MRP}}^{\mathrm{HS}}$ and $\mu_{\mathrm{MRP}}^{\mathrm{HS}}$ take the form

$$k_{\mathrm{MRP}}^{\mathrm{HS}} = k_{\mathrm{MRP}}^{\mathrm{HS}}\left(\mu_0, \left\{\mu_\lambda^i, \forall i \in [2, L_\lambda + 1], \forall \lambda \in [1, P]\right\}, k^0, \mu^0\right), \quad (33)$$

$$\mu_{\mathrm{MRP}}^{\mathrm{HS}} = \mu_{\mathrm{MRP}}^{\mathrm{HS}}\left(\mu_0, \left\{\mu_\lambda^i, \forall i \in [2, L_\lambda + 1], \forall \lambda \in [1, P]\right\}, k^0, \mu^0\right). \quad (34)$$

These expressions are rather complex, but fully analytical and exact, so that their computation does suffer from any numerical approximation. To our best knowledge, such an exact analytical solution to the auxiliary problem with spherical pores is available only for isotropic elasticity and for composite inclusions with spherical concentric layers. The restriction to isotropic behavior has led to the choice of the variational approach instead of other linearization procedures of the local nonlinear behavior such as the affine or the recent second-order approaches for which the elastic moduli of the LCC are anisotropic. Furthermore, due to the requirement of a spherical shape for the composite inclusions, the present analytical treatment can only be applied to porous materials with an isotropic distribution of pores. Last, since the layers should be concentric, a discretization of the matrix layers along the ortho-radial direction into spherical sectors, where each sector is characterized by an independent secant modulus, cannot be achieved analytically. Such a discretization could have accounted for the plastic gradient near the pores, not only in the radial direction but also in the hoop direction.

Eqs. (33) and (34) provide the additional expressions required to solve the nonlinear system (17) and (13). The results depend on the choice of reference medium:

- When $k^0 = +\infty$ (10^{30} in practice) and $\mu^0 = \max_{i,\lambda} \mu_\lambda^i$ the obtained yield surface is the generalized nonlinear Hashin–Shtrikman upper bound of the effective yield surface.
- When k^0 and μ^0 are much larger than the moduli of the layers (again 10^{30} in practice), the obtained yield surface is the generalized Voigt upper bound of the effective yield surface, which is less restrictive than the previous bound but does not require that the pores be isotropically distributed.
- Generalized self-consistent estimates of the yield surface are obtained when $k^0 = k_{\mathrm{MRP}}^{\mathrm{HS}}$ and $\mu^0 = \mu_{\mathrm{MRP}}^{\mathrm{HS}}$.
- The yield surfaces obtained with the lower generalized linear Hashin–Shtrikman bound and the generalized linear Reuss bound coincide because $\min_{i,\lambda} \mu_\lambda^i = 0$ (taken equal to 10^{-30} in practice). It is in general not a lower bound but provides another estimate.

2.4. Computation of second-order moments

Due to the complexity of the closed-form solution of the auxiliary problem which is based on a recurrence relation (see Hervé and Zaoui, 1993), closed-form expressions for the derivatives of the effective moduli with respect to the phase moduli in Eq. (17) are not available. Accordingly, these derivatives are computed numerically as a centered difference

$$\frac{\partial \mu^{\mathrm{eff}}}{\partial \mu_r} = \left[\mu^{\mathrm{eff}}(\ldots, \mu_r(1 + h/2), \ldots) - \mu^{\mathrm{eff}}(\ldots, \mu_r(1 - h/2), \ldots)\right]/(h\mu_r) \quad (35)$$

where h can be chosen small, typically equal to 0.001 or 0.0001, thanks to the precise analytical evaluation of μ^{eff}. At this stage it might be worth noting that the second-order moments from which the secant moduli are computed are given by $(\langle\varepsilon^2_{\text{eq}}\rangle_i)^M_\lambda = \frac{1}{N_\lambda}\sum_{k=1}^{N_\lambda}\langle\varepsilon^2_{\text{eq}}(\cdot + \boldsymbol{X}^k_\lambda)\rangle_i$, where $\boldsymbol{\varepsilon}$ is the local field in the LCC. Another "modified secant extension based on second moments" could be generated by using as reference strains the quantities $\langle[\varepsilon^M_\lambda(\cdot)]^2_{\text{eq}}\rangle_i$, i.e., the second moments of the strain in the auxiliary composite inclusions. This quantity admits an analytical expression (Bardella, 2003) but does not coincide with the variational procedure of Ponte Castañeda (1992) and does not provide bounds. In general it generates stiffer predictions since $(\langle[\varepsilon^M_\lambda(\cdot)]^2_{\text{eq}}\rangle)_i \leqslant (\langle\varepsilon^2_{\text{eq}}\rangle_i)^M_\lambda$. A more detailed discussion about the differences between these formulations and other formulations based on first moments can be found in Bardella (2003).

Because of these numerical differentiations, the present treatment is referred to in the sequel as a "semi-analytic model". However, the computational cost of the derivatives calculation is low. In addition, the low sensitivity of the parameter h on the results could systematically be checked. The nonlinear system of Eqs. (17) and (13) is in most cases solved by means of a fixed-point iterative procedure. The associated convergence criterion is defined by

$$\eta = \sqrt{\sum_{\lambda=0}^{P}\sum_{i=1}^{L_\lambda+1}\left[\frac{p^{k+1}_{\lambda,i} - p^k_{\lambda,i}}{\sup[(p^{k+1}_{\lambda,i} + p^k_{\lambda,i})/2, A]}\right]^2}, \tag{36}$$

with $p_{\lambda,i}$ the second-order moment of the strain rate in layer i of pattern λ and the constant A typically 0.01 times the largest $p_{\lambda,i}$. Superscript k stands for the iteration number. Typically, η ranges from 10^{-6} to 10^{-8} in the ensuing calculations. The determination of the self-consistent estimates requires an additional iterative procedure for the determination of the effective elastic moduli as a function of the secant moduli; another fixed point iterative procedure is used, with a criterion based on the relative discrepancy between the moduli of successive iterations, typically required to be below 10^{-8}.

The fixed point algorithm for the determination of the $p_{\lambda,i}$ works well for the models in which the reference medium is fixed (upper Voigt bound, lower Reuss and HS estimates) and for the self-consistent scheme, even if for the later the computations are somewhat longer because of the double iteration loops. However it turned out to be unstable for the Hashin–Shtrikman upper bound, for the following reason. Let

$$\mu^{\text{HS+}}_{\text{MRP}}(\mu_1, \ldots, \mu_S) = \mu^{\text{HS}}_{\text{MRP}}\Big(\mu_1, \ldots, \mu_S, \mu^0 = \sup_s \mu_s\Big)$$

be the general expression of the linear HS upper bound. Its derivations with respect to μ_s involves two terms

$$\frac{\partial \mu^{\text{HS+}}_{\text{MRP}}}{\partial \mu_r} = \frac{\partial \mu^{\text{HS}}_{\text{MRP}}}{\partial \mu_r} + \frac{\partial \mu^{\text{HS}}_{\text{MRP}}}{\partial \mu^0}\frac{\partial \mu^0}{\partial \mu_r}.$$

The last partial derivative vanishes when phase r is not the stiffest one and is equal to 1 otherwise. Since $\partial\mu^{\text{HS}}_{\text{MRP}}/\partial\mu^0$ is positive, the difference between the second-order moments computed when phase r is the maximum and when it is not, is significant. This induces infinite loops in the fixed point algorithm, as illustrated in the following typical example. Assume that the second-order moment of the strain rate decreases from the inner to the outer layer, but that the difference between the two last layers is small. The last layer will determine the reference medium and the above derivative will involve both terms, while for the previous layer only the first term will be relevant. As a consequence, the new secant moduli of the last layer will be smaller than that of the previous layer, which will determine the reference medium in the subsequent iteration. For the same reason, the last layer might become again the stiffest in the next iteration.

To overcome these difficulties, various strategies have been tested. Two of them turned out to be more efficient and are briefly described here:

- In the first approach, when the stiffest layer is not the last layer of a given pattern, all layers between the stiffest and the last layer are merged together into a single but thicker layer. This very simple approach allowed to generate upper bounds in many cases. It tends to reduce the efficiency of the radial discretization, but only to a limited extend since layers are only merged together when the radial strain rate gradients are small, in which case the effect of an additional discretization would have been small. This procedure does however not work when the reference layer "jumps" from one pattern to another.

- The second procedure consists in regularizing the supremum function so that the second part of the derivative is involved not only for the stiffest layers, but also for the layers with moduli close to the maximum. The reference medium μ^0 is defined as the solution $\bar{\mu}$ of the following equation

$$\sum_{\lambda=0}^{P} c_\lambda \sum_{i=1}^{L_\lambda+1} f_\lambda^i \left(\frac{\langle \mu \rangle_m}{\bar{\mu} - \mu_\lambda^i} \right)^\alpha = \frac{1}{\beta^\alpha}, \tag{37}$$

where α and β are positive constants to be chosen and $\langle \mu \rangle_m$ is the average of the secant moduli on the matrix. The modulus $\bar{\mu}$ depends on all local moduli and is always above the supremum so that the generalized Hashin–Shtrikman estimates obtained with $\mu^0 = \bar{\mu}$ is always an upper bound. When β tends to 0, $\bar{\mu}$ tends to the maximum but the nonlinear solution may not be found. On the other hand, larger values of β stabilize the fixed point algorithm but generate less stringent upper bounds. When all secant moduli are equal, β gives the relative discrepancy between the supremum and $\bar{\mu}$. Typical values of β for which convergence could be reached range from 0.001 to 1.

Note finally that for a given local porosity distribution, all possible discretizations of the patterns into layers and all choices of α and β generate upper bounds for the yield surface. The best one is obtained as the minimum of all generated surfaces. Unless otherwise specified, the results given in the next section are these optimal surfaces. They are not exactly equal to the theoretical best Hashin–Shtrikman type upper bounds, but it is highly likely that they are very close to these.

3. Macroscopic yield surface of a porous material

In this section, the new nonlinear variational generalized Voigt upper bound (referred to as VgVb), Hashin–Shtrikman upper bound (VgHSb), self-consistent estimate (VgSCe) and Reuss estimate (VgRe) are compared to earlier predictions, in the simplest morphological situation in which the local pore volume fraction is not constant, that is, for a microstructure described by two patterns ($P = 2$). The macroscopic porosity is set to $f = 10\%$ while the local porosities, f_1 and f_2, and the pattern volume fractions, c_1 and $c_2 = 1 - c_1$, which satisfy Eq. (27), are arbitrary. Since the obtained improvements are two-fold, being due both to the discretization into layers and to the explicit use of local pore volume fractions, and in view of separating these effects, we consider first the situation of a single pattern, (i.e., $f_1 = f_2$). Corresponding results are essentially those already given by Bilger et al. (2002) for a lower porosity and serve as references for comparisons with predictions involving porosity fluctuations. Some additional comparisons with other recent results are also performed. In a second step, the new predictions are given for fixed ratios $\xi = f_2/f_1$ and $\psi = c_2/c_1$, equal to 1/3 and 1, respectively, and compared to the reference situation. Finally, more general morphological situations are explored by varying these ratios; earlier results are recovered as limiting cases.

3.1. Classical composite spheres assemblage

The four predictions of the macroscopic yield surfaces resulting from the present analysis are compared in Fig. 6 to earlier bounds and estimates relative to a classical CSA. The matrix has been discretized into 30 layers with uniform thickness for the computation of the VgVb, VgSCe and VgRe curves while 20 layers have been used for the VgHSb at high triaxiality, and progressively reduced to 9 thin inner layers and one thick outer layer for $\tau = 0$ according to the layer-merging procedure described at the end of previous section, which turned out to predict the most restrictive bounds in this case. The predictions of the alternative regularization procedure were however very close, with relative discrepancies below 10^{-3}. In the standard ($\Sigma_{\rm eq}$, Σ_m) plane used in Fig. 6(a), discrepancies between the various results are hard to distinguish since all are close to the Gurson curve. That is why in (b), curves are given in "normalized polar coordinates" $(r/r_G, \theta)$, where the polar angle θ is directly linked to the triaxiality ratio according to $\tan(\theta) = \tau$ and the radius $r = \sqrt{\Sigma_m^2 + \Sigma_{\rm eq}^2}$ is divided by the radius $r_G(\theta)$ of the Gurson prediction for the same triaxiality. Among all these curves, the HS bound is the most general since it applies to any microstructure with an isotropic distribution of pores. The Gurson, Gãrãjeu–Suquet and VgVb upper bound are based on exactly the same microstructural assumptions, since they are relative to a CSA with uniform local porosity and no particular assumption

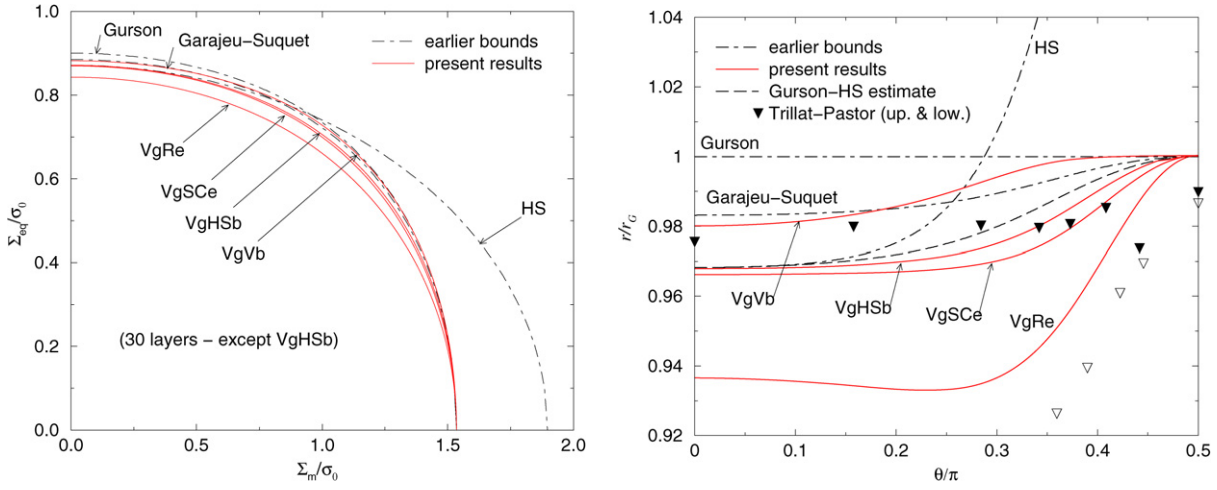

(a) (b)

Fig. 6. Comparison between earlier upper bounds of the macroscopic yield surface and present generalized variational predictions: Voigt and Hashin–Shtrikman upper bounds, self-consistent and Reuss estimates. Curves in the $(\Sigma_{\rm eq}, \Sigma_m)$ plane (a) and in the $(r/r_G, \theta/\pi)$ plane (b). Gurson-HS model and numerical results of Trillat and Pastor (2005) are added in (b). CSA: global porosity $f = 10\%$.

on the spatial distribution of the pore centers. The data recently obtained numerically by Trillat and Pastor (2005, Table 3) are relative to the same situation. Their kinematic results relative to a homogeneous strain loading (column 4) and their static data relative to imposed uniform tractions (column 6) can easily be interpreted as (numerical) upper and lower bounds relative to this morphological situation. They are reported in Fig. 6(b) as well. Both Gãrãjeu–Suquet and VgVb bounds improve on the Gurson model at any triaxiality, with an improved performance of the VgVb bound at low triaxiality, up to $\theta = 0.2\pi$, where it is very close to the numerical result. At intermediate and high triaxiality, the Gãrãjeu–Suquet bound improves on the VgVb but both deviate from the numerical simulations, probably because of complex nonlinear local interactions which cannot be addressed by the essentially linear solutions which determine the trial fields used to derive these bounds. At infinite triaxiality, all predictions coincide since the Gurson model is an exact result in this particular case. The variational generalized models converge to this model as soon as the number of layers is sufficient, as shown by Bilger et al. (2002). In the present case with $f = 10\%$ and 30 layers, the predictions of the semi-analytical models overestimate the Gurson model at $\tau = +\infty$ by less than 3×10^{-4}. Indeed, under pure hydrostatic load and because of the spherical symmetry of the inclusion problem, the local fields in the matrix shell are radial, with a displacement fluctuation varying as ρ^{-2} (where ρ is the distance to the pore center), and a strain varying as ρ^{-3}, whatever the isochoric constitutive relation. The local secant modulus then varies as $\sigma_0\rho^3$, with no fluctuation within a layer nor from one pattern to the other, so that the secant moduli in a layer are indeed equal to the local secant moduli. As a consequence, the local strain but also stress fields in the LCC are the exact fields in the nonlinear problem. It is however noticeable that the numerical solution of Trillat and Pastor (2005), even if the upper and lower bounds are very close, slightly underestimates the Gurson result. This is probably the consequence of the imperfect geometrical approximation of the spherical matrix shell with pyramidal elements, and illustrates the difference between a fully numerical approach and the present semi-analytical computations which do not suffer from such approximations. In addition, the present simulations require much less computational power, with about 30 unknown secant moduli to be optimized, to be compared with several ten-thousands of degrees of freedom.

When in addition the pore centers are assumed to be isotropically distributed in space, the VgHSb applies and improves on all other analytical bounds at all triaxiality and on the numerical results up to $\theta \approx 0.35\pi$. It is very close to the latter for higher triaxiality, the small discrepancy being close to the above mentioned possible numerical errors of the numerical data. The Gurson-HS estimate turns out to be slightly too stiff with respect to our bound, but is very close to it, as already noticed by Bilger et al. (2002) for a lower porosity, and could be seen as a good and improved substitute to the Gurson model in structural calculations, in view of its very simple close-form expression. The generalized self-consistent estimate is slightly softer than the VgHSb upper bound at all triaxiality ratios. It deviates significantly from the classical HS upper bound at $\tau = 0$, while the VgHSb bound remains very close to it,

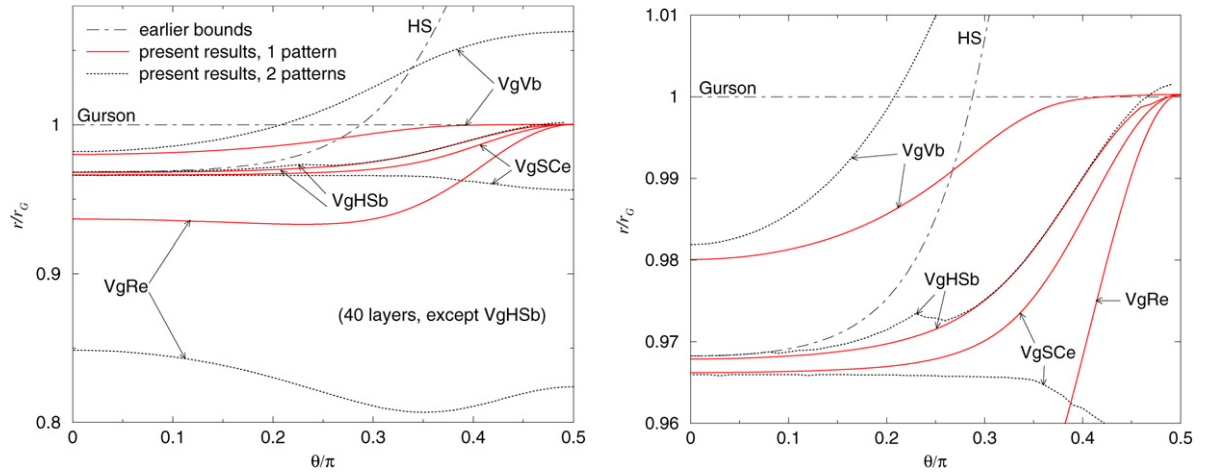

Fig. 7. Comparison between predictions based on one and two patterns. Full curves in the $(r/r_G, \theta/\pi)$ plane (a) and enhanced zoom on the VgHSb and VgSCe curves (b). Global porosity is 10%, local porosities are 5% and 15%.

with less than 4×10^{-4} relative discrepancy. At this stage it is not clear whether this difference is significative or is the consequence of the slight errors induced by the numerical computation of the second-order moments. On the other hand, the VgRe is significantly softer than all other predictions, but still above the numerical lower bound of Trillat and Pastor (2005) (which tends to $0.884 r_G$ at $\theta = 0$), consistently with the fact that the VgRe is not a bound, except for $\tau = +\infty$.

3.2. Effect of local porosity fluctuations: simple case

We consider now a microstructure described with two patterns such that $f_1 = 15\%$, $f_2 = 5\%$, $c_1 = c_2 = 50\%$ and compare, in Fig. 7, the predictions of the proposed models in this situation, referred to with the subscript "het", e.g. $\mathrm{VgVb_{het}}$, with those obtained in the previous more classical situation, referred to with the subscript "hom".

Consider first the generalized Reuss estimate. It appears clearly to be much softer when local porosity fluctuations are considered instead of the global one, whatever the triaxiality ratio. Indeed it can easily be checked that the $\mathrm{VgRe_{het}}$ estimate of an assemblage made of patterns with variable local porosity, is the $\mathrm{VgRe_{hom}}$ estimate of the CSA made of patterns with uniform porosity equal to the largest local porosity. This is the consequence of the fact that uniform and identical tractions are imposed at the boundary of all patterns describing the LCC, among which only one, namely the one with the largest porosity, undergoes plastic flow and controls the overall load, all other being rigid, with arbitrarily large secant moduli. The $\mathrm{VgRe_{het}}$ curve in Fig. 7 can be numerically checked to coincide with the $\mathrm{VgRe_{hom}}$ estimate of the classical CSA with 15% porosity. As previously, this curve is not a lower bound for the effective yield surface. It could however be easy to generate rigorous lower bounds for a multi-pattern CSA from Reuss-type lower bounds for classical CSA, such as those derived numerically by Trillat and Pastor (2005), by taking the intersection of all yield surfaces of the individual pattern. The corresponding admissible stress fields would be obtained by juxtaposition of the local stress fields used to derive the lower Reuss bounds for the CSA with homogeneous porosity: they are plastically admissible and locally balanced by construction and satisfy the global equilibrium since the stress vectors are identical at the boundary of the patterns. This holds in particular for a purely hydrostatic load, for which the Gurson prediction is an exact result and thus a lower bound for a CSA with uniform porosity. The Reuss lower bound for a generalized CSA at infinite triaxiality, which is no longer an exact prediction, reads then

$$\Sigma_0^R = \inf_{\lambda=1,\dots,P} \sigma_0^\lambda \quad \text{with } \sigma_0^\lambda = -\frac{2}{3}\sigma_0 \ln(f_\lambda), \tag{38}$$

where σ_0^λ is the hydrostatic pressure that induces plastic flow in the CSA made of patterns with porosity f_λ. As a corollary, the $\mathrm{VgRe_{het}}$ of a microstructure described by the Voronoï or the Stienen model is essentially controlled by the Voronoï cell with the highest local porosity and, respectively, the pore that has the closest first neighbor.

On the other side, the Voigt bound of a CSA with nonuniform local porosity is less restrictive than the corresponding $\mathrm{VgVb_{hom}}$ bound with same overall porosity. The discrepancy is small at low triaxiality, where the $\mathrm{VgVb_{het}}$ remains below the Gurson bound. At high triaxiality, it is significantly above the Gurson model. As for the Reuss type bound, it is rather easy to generate the $\mathrm{VgVb_{het}}$ from the $\mathrm{VgVb_{hom}}$ bounds, relative to all the local porosities f_λ. Indeed local fields in the composite inclusions are decoupled from each other as a consequence of the prescription of the overall homogeneous velocity at their boundary, so that they can be solved independently. The overall Voigt dissipation potential is then obtained by averaging the local Voigt dissipation potentials of each individual pattern, weighted by their volume fraction c_λ. Graphically, the points on the $\mathrm{VgVb_{het}}$ yield surface are the weighted averages of the points on all $\mathrm{VgVb_{hom}}$ yield surfaces that have the same outer normal. This averaging is particularly simple on the axis $\Sigma_{\mathrm{eq}} = 0$ and $\Sigma_m = 0$, where the normals to all surfaces coincide. In the first case, one gets the Voigt upper bound under pure hydrostatic load

$$\Sigma_0^V = \sum_{\lambda=1,\ldots,P} c_\lambda \sigma_0^\lambda. \tag{39}$$

The strong dependence of this quantity with the heterogeneity of the local porosity is a consequence of the strong nonlinearity of the logarithm function. The concavity of the latter ensures that the $\mathrm{VgVb_{het}}$ bound at infinite triaxiality is always equal to or larger than the Gurson estimate. Similarly, under purely deviatoric load, the $\mathrm{VgVb_{het}}$ limit is the weighted average of the $\mathrm{VgVb_{hom}}$ limits under pure deviatoric loads. A linear variation of the latter with porosity would induce an independence of the $\mathrm{VgVb_{het}}$ limit with respect to local porosity fluctuations. The observed slight evolution suggests that the dependence is not linear, but probably not far from linear. Note that a simple generalization of the Gărăjeu–Suquet bound to a heterogeneous local porosity distribution could be obtained in the same way. It would generate the same result as the $\mathrm{VgVb_{het}}$ bound for infinite triaxiality and only a small dependence on local porosity fluctuations at low triaxiality, since the $\tau(f)$ coefficient involved in Eq. (46), which determines the flow stress under deviatoric stress, is only slightly nonlinear in f.

While simple and exact connections between the Voigt and Reuss-type predictions for classical CSAs with uniform local porosity and for generalized CSAs with heterogeneous distributions of local porosity can be established, these results can hardly be considered as efficient assessments of the effect of local porosity fluctuations on the effective strength domain, since the evolution of both predictions are opposite and, more importantly, the mechanical interactions between patterns are totally switched out within such approaches. This is not the case of Hashin–Shtrikman type models, such as the VgHSb and the VgSCe, which explicitly rely on an assumption on the relative position of the pattern centers. It turns out, as can be observed in Fig. 7(b), that the $\mathrm{VgHSb_{het}}$ prediction is slightly above the $\mathrm{VgHSb_{hom}}$ curve, but with a discrepancy which seems to be mostly due to the convergence problems discussed at the end of Section 2.4. The plotted $\mathrm{VgHSb_{het}}$ curve exhibits two branches separated by a little local peak. The left branch (low triaxiality) has been obtained with the algorithm using the regularized supremum function, while the right branch results from the layer-merging procedure. It is likely that if more sophisticated algorithms had been used to get even closer to the optimal Hashin–Shtrikman bound, the $\mathrm{VgHSb_{het}}$ and $\mathrm{VgHSb_{hom}}$ predictions would have been very close, as suggested by the fact that they are almost indistinguishable in areas where convergence problems where not acute, such as for θ around 0.35π. Such a result would extend to nonlinear behavior the corresponding one relative to linear properties: it is clear from the identity of the auxiliary composite inclusion problem (pore embedded in matrix embedded in reference medium with properties identical to those of the matrix), that the linear pattern-based Hashin–Shtrikman upper bound is not sensitive to local porosity fluctuations. The possible extension of such a result to nonlinear properties deserves additional theoretical analyses, which are left for further investigations.

Even if this result would not be rigorously true, it seems anyway that the local porosity fluctuations have only a very limited effect on the VgHSb bound. A short interpretation of this observation would conclude to the independence of the effective strength domain with respect to this morphological parameter, which would not be consistent with the results of full-field numerical simulations (Bilger et al., 2005). It should however be recalled that the VgHSb prediction is a rigorous upper bound, supposed to be valid for any morphological configuration. As such it describes an extreme situation which is highly unlikely, and might even not exist, since the attainability of the HS pattern-based bounds has not yet been established in a general situation. Its practical pertinence as a prediction of effective properties is thus questionable, especially when subtile effects, such as the porosity fluctuations under consideration, are to be analyzed. That is why self-consistent estimates are preferred. Even if the morphological situations such estimates

describe are not clearly known, they do not suffer from the above restriction and are likely to represent a real situation. In addition, their construction induces interactions between patterns, through the infinite effective reference medium, which are stronger than those involved in upper HS bounds and are likely to emphasize the morphological effects under investigation. Indeed the obtained results show a softening of the effective properties when porosity fluctuations are taken into account, especially at high triaxiality ratios ($\theta \geqslant 0.3\pi$), with a discrepancy between $\mathrm{VgSCe_{hom}}$ and $\mathrm{VgSCe_{het}}$ up to 5%, which is in qualitative agreement with the trends observed on numerical simulations (Koplik and Needleman, 1988; Bilger et al., 2005), which show that the Gurson model is too stiff, especially at large triaxiality ratios. This effect is clearly due to porosity fluctuations since this is the only difference between the $\mathrm{VgSCe_{hom}}$ and $\mathrm{VgSCe_{het}}$ predictions, and could be assessed by the self-consistent model because of the enhanced description of the interaction between patterns with respect to the $\mathrm{VgHSb_{het}}$ bound: plastic flow concentrates more in the weak pattern in the $\mathrm{VgSCe_{het}}$ than in the $\mathrm{VgHSb_{het}}$ predictions. The lower dependence on porosity fluctuations at low triaxiality ratios is probably due to a poorer description of the local plastic flow under these conditions, where the main heterogeneities are no longer radial but along the hoop direction. Indeed it can be checked that the radial discretization does not have a strong effect on self-consistent predictions at low triaxiality, similarly to what was observed by Bilger et al. (2002) for the classical CSA. A further softening of the yield surface would require a discretization along the ortho-radial direction in order to take better into account the actual local strain rate gradient. Such an improved description of the plastic behavior would probably also induce an improved analysis of the effects of the porosity fluctuations under such conditions. This can however not be performed with the analytical solutions at hand and would require numerical computations, which are left for further investigations.

3.3. Self-consistent predictions of the effect of the heterogeneity of the local porosity

We conclude this section by a more systematic analysis of the influence of parameters ξ and ψ on the VgSCe predictions. Most following results were obtained with a discretization of the matrix of each pattern into 20 layers, which turned out to be sufficient. We first set $\psi = 1$ as in the previous particular case and investigate the effect of the contrast between the local porosities, with ξ varying from 0 to 1. These extreme cases are illustrated in Fig. 8. For $\xi = 1$, the porosity distribution is uniform and the generalized Hashin CSA simplifies into the classical Hashin CSA. For $\xi = 0$, the porosity distribution is highly heterogeneous. The second pattern is only made up of matrix ($f_2 = 0$) and represents the matrix in the RVE outside the domains represented by the first pattern. In Fig. 9, the VgSCe for the effective yield surfaces is plotted for different ξ values in the standard (Σ_{eq}, Σ_m) plane. It is compared with the Gurson bound and the Gurson–Tvergaard estimate (GT) for which q has been set to 1.25, to obtain a good fit with our model for $\xi = 0$. Whatever the value of the porosity contrast ξ, the VgSCe is always softer than the Gurson bound. It is noted that the stiffest and softest yield surfaces correspond to a uniform or highly heterogeneous porosity distribution, respectively. Furthermore, an increase in the porosity contrast implies a softening increase in the yield surface, especially for large triaxiality factors. Nevertheless this softening effect as predicted by this model should not be considered as a general result as discussed below. The similarity between the VgSCe for $\xi = 0$ and the GT estimate

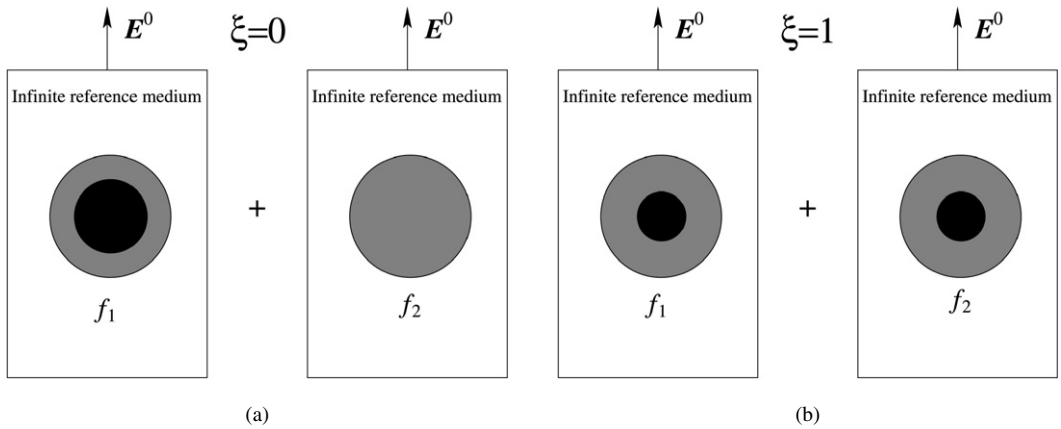

Fig. 8. Auxiliary problems to solve. In (a) $\xi = 0$; in (b) $\xi = 1$.

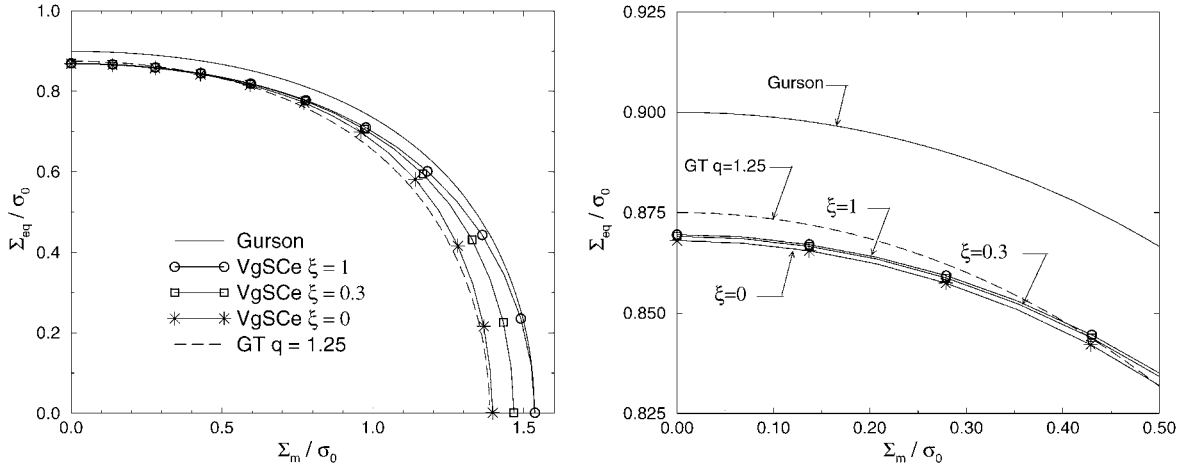

(a) (b)

Fig. 9. Influence of the porosity contrast ξ on VgSCe predictions (a). Zoom for low triaxiality factors (b) $\psi = 1$.

with $q = 1.25$ is clear, even if both models result from very different analyses: a fit on numerical data relative to periodic microstructures for the GT model and the proposed nonlinear homogenization model for the VgSCe, which in principle does not rely on any fitting parameter since the local porosities and their volume fractions can be deduced from the microstructure as described in Section 2.2.3.

The porosity contrast ξ is now set to zero and the contrast between the pattern volume fractions ψ is evolving. The analysis is focused on the response under hydrostatic load ($\tau = +\infty$), where the morphological effects are the most important. It is noted that when $\xi = 0$ and $c_2 > 0$, the microstructure is described by composite patterns with a local porosity equal to $f_1 > f$, the centers of which need to be assumed to be isotropically distributed to satisfy the assumptions of the VgSCe, embedded in a homogeneous matrix represented by the homogeneous pattern present in proportion c_2. No particular statistical assumption is required for the centers of this homogeneous pattern, which can be interpreted as the fictitious pattern representing the matrix outside actual patterns, as described in Section 2.2.1. Similarly, microstructures with $c_2 > 0$ do not require the fractal construction of the classical CSA and are likely to represent more accurately real porous materials. When $\psi = 0$ the whole matrix phase is contained in the first pattern and the microstructure coincides with the classical CSA. When ψ reaches its maximal value, which can easily be checked to be $\psi_{\max} = \frac{1}{f} - 1$ since $f_1 = \frac{1+\psi}{1+\xi\psi} f \leqslant 1$, all the matrix is contained in the homogeneous second pattern and the first pattern is made of voids only, without matrix shell. In intermediate situations, the ratio $c_2/(1-f) = \psi/(1-f)(1+\psi)$ gives the proportion of matrix phase that is contained in the second pattern, that is the matrix that is not associated with a neighbor pore. This ratio evolves from 0 to 1 when ψ goes from 0 to $\psi_{\max}$. The evolution of the macroscopic flow stress under hydrostatic load $\Sigma_m(\tau = +\infty)$ as a function of $c_2/(1-f)$ is depicted in Fig. 10. A strong dependence is observed. Up to $c_2/(1-f) = 0.9$, i.e., for microstructure in which at least 10% of the volume occupied by the matrix can be associated with a pore within a composite pattern, the VgSCe is able to capture the main trend observed by various numerical simulations, that is an effective hydrostatic yield stress significantly below the prediction of the Gurson model. The maximum drop is observed when about 40% of the matrix is associated with pores and it reaches about 10% of the Gurson prediction. This is a significative softening, which can be interpreted as the consequence of the fact that within such microstructures, pores can get closer to each other than in the classical CSA. Weak local path connecting the pores to each other can exist and may induce strain localizations that limit the overall resistance of the porous composite. However, for $c_2/(1-f) > 90\%$, the VgSCe leads to stiffer predictions for Σ_m than the Gurson bound. This is the consequence of the preponderant contribution of the homogeneous pattern. Indeed, the local fields in the corresponding auxiliary problem are homogeneous. This can be checked from the general equations of this problem which essentially is a classical Eshelby type problem with a linear infinite medium and a nonlinear inclusion, for which it is known that local fields are homogeneous in the inclusion. From a more fundamental point of view, this is also the consequence of the fact that this homogeneous pattern represents the matrix not associated with a pore within a heterogeneous pat-

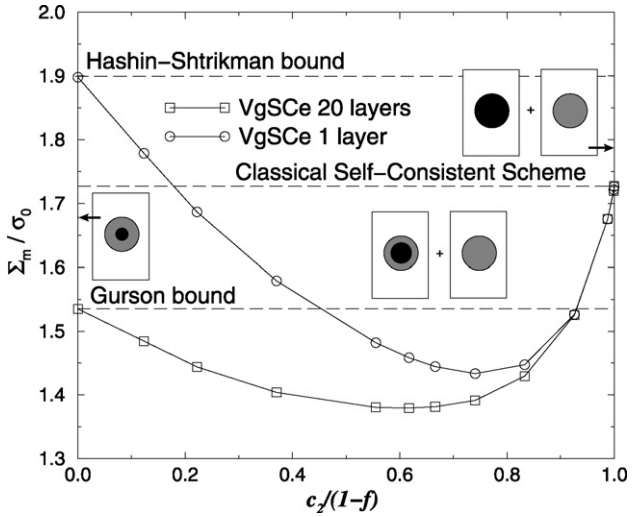

Fig. 10. Variation of the normalized macroscopic hydrostatic stress Σ_m/σ_0 derived from the VgSCe as a function of the ration $c_2/(1-f)$ for $\xi = 0$.

tern. All points in this surrounding matrix are handled similarly during the scale transition, as in the classical "point approach", so that only global statistical informations can be obtained for this subphase, without explicit spatial dependence. While this does not mean of course that local fields are homogeneous in the RVE, it does however not allow to use a nonuniform distribution of secant moduli within the proposed modeling framework. The homogeneity of the field in this pattern is also confirmed by the independence of the VgSCe with respect to the discretization into layer for $c_2 = 1 - f$: predictions obtained with 20 layers or only one layer do coincide, and can be checked to coincide with the predictions of the classical self-consistent scheme, since the corresponding auxiliary problems are identical. For slightly lower c_2, the predictions are also almost independent on the discretization, as a consequence of the homogeneity of the fields in the second auxiliary problem, and the quasi homogeneity of the secant moduli in the matrix of the composite pattern. Indeed this pattern is then made of a pore surrounded by a thin matrix layer, where the secant moduli which, as mentioned in Section 3.1, evolve as $\sigma_0\rho^3$, are almost constant. On the other hand, for low and intermediate c_2, the discretization has a strong influence. For instance, as already pointed out by Bilger et al. (2002), it induces a drop from the Hashin–Shtrikman bound to the Gurson prediction at $c_2 = 0$. Note that in that case the VgSCe obtained with one layer coincides with the standard variational nonlinear extension of Christensen and Lo's three-phase model, based on the use of a single secant moduli for the matrix, which itself coincides with the Hashin–Shtrikman bound for infinite triaxiality, since both models are then exact results in the linear case.

The drop of the VgSCe with respect to the Gurson prediction for intermediate values of c_2 is significative, and of primary importance, since, as noted at the beginning of this section, the microstructure described by the VgSCe is likely to be more realistic with respect to real microstructures than the classical CSA. The stiffer prediction at high values of c_2 is the consequence of the poor assessment of the local plastic strain gradients and corresponding secant moduli fluctuations. Anyway, the present model improves significantly on the Gurson model for intermediate values of c_2, and could therefore be used as a substitute to it. Its main limitation is its complex formulation and the iterative loops required to optimize the set of secant moduli. Its computation is however much faster than fully numerical micromechanical simulations: a point of the strength domain at a fixed triaxiality ratio can be obtained within a fraction of a second on a standard laptop computer, and this time is likely to be reduced significantly if more efficient optimization procedures would be used. In addition, the simplified model based on a single layer in the pattern, with only two secant moduli to be optimized and which is likely to be given an almost fully analytical expression thanks to the simpler expressions of the local fields in the matrix of the composite inclusion, can be computed much faster. It provides predictions not so far from the fully discretized model for intermediate values of c_2, and at least significantly below the Gurson prediction for $c_2/(1-f) \in [0.5; 0.85]$.

4. Comparison with full-field computations

In order to evaluate both the relevance and the limitations of VgSCe, this section aims at comparing the macroscopic yield surfaces obtained by the VgSCe with those derived from simulations on realistic three-dimensional microstructures. Both the present treatment and the numerical calculations, based on a technique making intensive use of fast Fourier transforms (FFT), are applied on the same simulated microstructure with multiple randomly distributed voids, the construction of which is described in Section 4.2.

4.1. Numerical simulations based on the Fast Fourier Transform

We only specify here the particularities of the application of the classical FFT method (Moulinec and Suquet, 1994; Moulinec and Suquet, 1998) to porous materials with a rigid-perfectly plastic matrix. For infinite contrast, which is precisely the case here for porous materials, the classical FFT method no longer converges since its rate of convergence is related to the contrast between the phases. This difficulty can generally be overcome by making use of an augmented Lagrangian method. The resulting saddle-point problem is then solved by Uzawa's algorithm Michel et al. (2000). For a rigid-plastic von Mises matrix, the nonlinear problem in the Uzawa algorithm described by Eq. (9) in Michel et al. (2000) is not smooth enough since the strain energy function $w(\boldsymbol{x}, \boldsymbol{\varepsilon}) = \sigma_0 \varepsilon_{\rm eq}$ cannot be differentiated at the origin. To overcome this difficulty, the strain energy function is regularized by adding an isotropic elastic term (Michel et al., 2000) in such a way that

$$w(\boldsymbol{x}, \boldsymbol{\varepsilon}) = \frac{9}{2} k \varepsilon_m^2 + f(\varepsilon_{\rm eq}) \quad \text{with } f(\varepsilon_{\rm eq}) = \begin{cases} \frac{3}{2}\mu \varepsilon_{\rm eq}^2 + \frac{\sigma_0^2}{6\mu} & \text{when } \varepsilon_{\rm eq} \leqslant \frac{\sigma_0}{3\mu}, \\ \sigma_0 \varepsilon_{\rm eq} & \text{when } \varepsilon_{\rm eq} \geqslant \frac{\sigma_0}{3\mu}, \end{cases} \tag{40}$$

where k and μ are the elastic bulk and shear moduli, respectively, and are chosen arbitrarily. The addition of the elastic term, which does not affect the yield surface of the porous material, is a numerical trick. The determination of the yield surface requires a step-by-step procedure which is fully described by Michel et al. (1999).

Three-dimensional microstructures with large unit cells such as the one we use in Section 4.3 to compare the present treatment with FFT simulations are close to being isotropic, since the statistical process by which they were generated does not select any preferential direction. The only source of geometrical anisotropy is the assumption of overall periodicity, but its effect is small as soon as sufficiently large unit cells, with respect to pore size, are considered. Since the matrix constitutive behavior, Eq. (40), is also isotropic, the effective behavior should therefore only depend on the three invariants of the overall stress $\boldsymbol{\Sigma}$, namely the mean stress Σ_m, the equivalent von Mises stress $\Sigma_{\rm eq}$ and the determinant $\det(\boldsymbol{\Sigma})$. In order to capture the effects of the third invariant of the stress, $\det(\boldsymbol{\Sigma})$, on the overall yield surface, generally plotted as function of $\Sigma_{\rm eq}$ versus Σ_m, two different types of loading, namely type-A loading and type-B loading, are considered. Both combine a hydrostatic load with, respectively, a pure shear and an axial symmetric traction:

$$\begin{cases} \boldsymbol{\Sigma} = \begin{pmatrix} T & R & 0 \\ R & T & 0 \\ 0 & 0 & T \end{pmatrix}, \quad R > 0: \quad \text{Type-A loading}, \\ \boldsymbol{\Sigma} = \begin{pmatrix} T & 0 & 0 \\ 0 & S & 0 \\ 0 & 0 & S \end{pmatrix}, \quad S > T: \quad \text{Type-B loading}. \end{cases} \tag{41}$$

For similar values of the first and second invariants, these loading types correspond to extreme values of the third invariant. For computational purposes, FFT calculations are performed with a discretization of the image of the unit cell into 64^3 voxels, the radius of a pore being about 2.1 voxels. Although this may seem relatively coarse, it proves to be sufficient. Indeed, the results obtained on the same microstructure discretized into 64^3 voxels and into 128^3 voxels differ by less than 0.5% in terms of the overall stress.

4.2. Simulation of three-dimensional microstructures

Although the experimental methods devoted to characterize microstructures have recently made lot of progress, it is still difficult to derive three-dimensional microstructures from real samples. Further, the obtention of general results

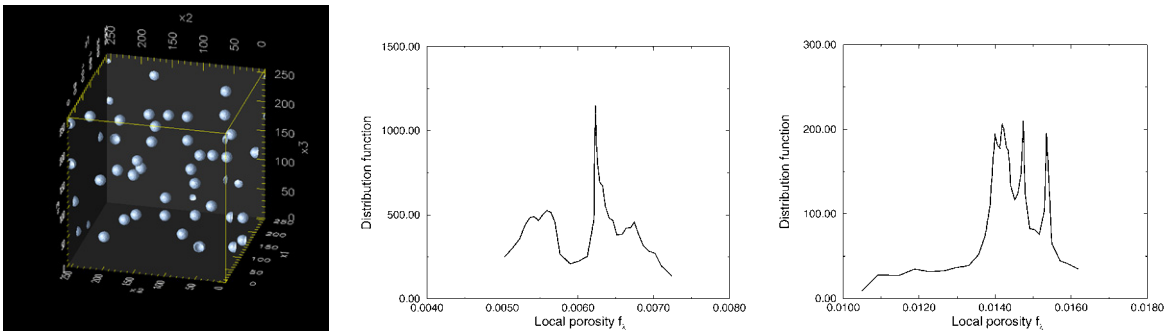

(a) (b) (c)

Fig. 11. (a) Periodic three-dimensional random microstructure generated by the cherry pit model ($d = 0.19$, $f = 0.6\%$). Distribution functions of the local porosity according to the Voronoï model (b) and the Stienen model (c).

which would not depend of specific details of a given microstructure requires to carry out numerical simulations on microstructures for which some statistical properties can be prescribed and precisely controlled. For these reasons, we chose to perform numerical simulations on simulated microstructures. Note that simulated microstructures should be periodic since the FFT method only applies to periodic problems. Several schemes can be used to generate random microstructures (Torquato, 2003). In this study, simulated microstructures consist of a homogeneous matrix containing spherical voids with same radius R, the centers of which are randomly implemented such that their distribution is isotropic within the unit cell. Three main different types of microstructure can be obtained, depending on the chosen restriction on the relative positions of the centers (Bilger et al., 2005). For the classical boolean model, no restriction is made on the latter so that voids can overlap. For the hard sphere model, the spheres are not allowed to overlap but still can come into contact. For the cherry pit model (Fig. 11(a)), a nonzero minimal distance d between the voids is prescribed, preventing both overlapping and contact. In this study, only the cherry pit model is considered. The spheres of the cherry pit model are randomly generated one after the other. If the new sphere does not fulfill the minimal distance requirement with respect to all previous spheres and their periodic reproductions, it is rejected and replaced by a new one until the constraint is satisfied. Periodicity of the microstructure is enforced by splitting spheres which intersect the edge of the image into 2, 4 or 8 parts. The parts which belong to the peripheral cells are moved into the main unit-cell by periodicity. The effective porosity can be monitored precisely. To this end, the pore radius is derived from the overall porosity, from the prescribed pore number and from the known volume of the RVE. The discrete voxels are associated to the matrix or void phase, depending on the distance of their centers with respect to the nearest pore center.

4.3. Semi-analytical predictions versus three-dimensional FFT simulations

Comparisons between the FFT simulations and the predictions of the semi-analytical model are performed on a single random microstructure comprising 39 spherical voids. The effective porosity and the minimal distance separating the edge of the pores are first set to $f = 0.6\%$ and $d = 0.19W$, respectively, where W is the size of the cubic unit cell. Each void contains 40 voxels when $W = 64$ voxels. From this microstructure, two different distribution functions of the local porosity can be obtained, depending on whether the Voronoï or the Stienen model, both described in Section 2.2.3, is used. They are reported in Figs. 11(b)–11(c). Remind that the generalized Hashin CSA is made up of 39 multilayer composite inclusions and one homogeneous pattern (representing the matrix outside the composite spheres as described in Fig. 4) for the Stienen model instead of only 39 multilayer composite inclusions with lower local porosities for Voronoï's one. For the considered microstructure, the concentration of the matrix only-made pattern attains 59% in the Stienen description. The matrix of each composite pattern is again discretized into 20 concentric layers and the convergence of the fixed point iterative procedure associated with the semi-analytical self-consistent model is attained for $\eta \leqslant 2 \times 10^{-8}$.

The effective yield surfaces derived from both the semi-analytic model applied to either a Voronoï or a Stienen porosity distribution and the three-dimensional FFT simulations, for a Type-A or Type-B loading, are depicted in Fig. 12. As can be seen in Fig. 12(b), the VgSCe derived from the Stienen model and the one derived from the

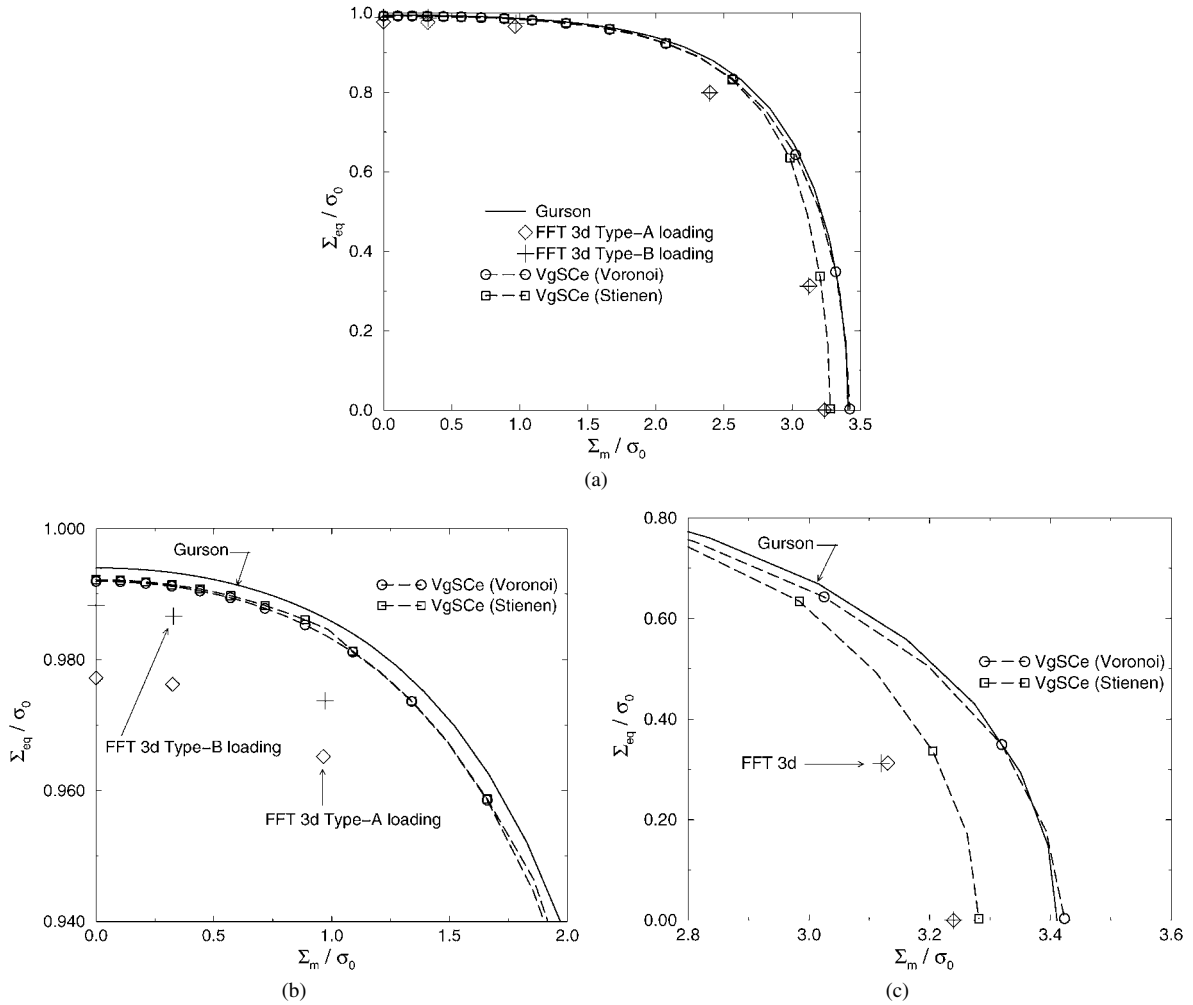

Fig. 12. Macroscopic yield surface. Comparison between the VgSCe (associated with either a Voronoï or a Stienen porosity distribution), the FFT simulations and the Gurson bound. Full curves (a) and zooms for low triaxiality factors (b) and large triaxiality factors (c).

Voronoï model are in very close agreement for low triaxiality factors, thus showing again that the porosity distribution does not have a significant influence on the effective yield surface in that case. Both VgSCe estimates are in good agreement with the FFT results for an axisymmetric load (type-B) at low triaxiality factors. The simulations relative to shear (type-A loading) show a slightly softer response. Let us recall (see Section 2.1.2) that, by construction, the VgSCe does not take into account the third invariant of the prescribed stress and then does not make any difference between type-A and type-B loadings. As a consequence it is not able to capture such an effect, which, as shown by the FFT simulations and for the microstructure we consider, remains however rather small. For a detailed discussion regarding the effect of the third invariant of the effective stress on the effective yield surface, the reader is referred to Richelsen and Tvergaard (1994) who have performed finite element simulations on a square unit cell consisting of a spherical void surrounded by a plastic matrix. For large triaxiality factors, the influence of the third invariant is even less pronounced and is no longer relevant for infinite triaxiality.

For such triaxiality factors, only the VgSCe associated with the Stienen porosity distribution is in good agreement with the FFT simulations which predict, as expected, a significantly softer hydrostatic yield stress than the Gurson model. This results from the fact that the Voronoï porosity distribution, unlike the Stienen one, is weakly heterogeneous and is therefore unable to efficiently take into account the porosity distribution in the microstructure, and especially the fact that some pores can come into close contact: indeed this feature seems to be the main softening mechanism as discussed in Section 3.3 while commenting the results of Fig. 10. This is also illustrated in Fig. 11(b)

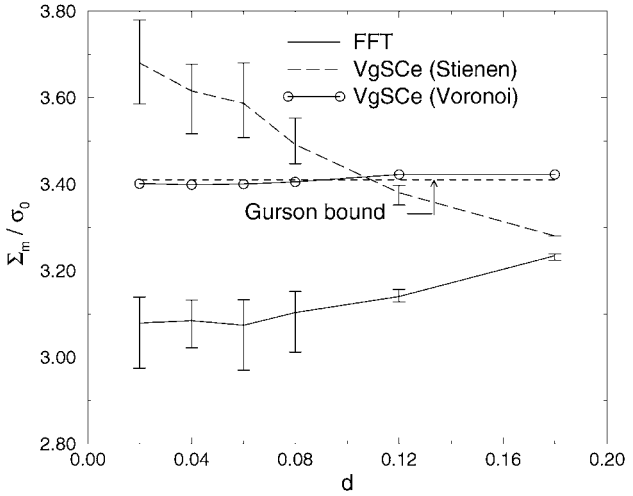

Fig. 13. Evolution of the normalized macroscopic hydrostatic stresses Σ_m/σ_0 derived from the VgSCe and from FFT simulations as functions of the minimal distance d.

where it can be observed that the width of the Voronoï porosity distribution is rather weak (0.2%) while the distribution of the local porosities of the composite inclusions in the Stienen model ranges from 1% to more than 1.6%. Note that the value of the Stienen distribution function at $f = 0$ has not been reported in Fig. 11(c) for visibility purposes.

As can be seen in Fig. 12(a), the largest discrepancy between the FFT simulations and the VgSCe is observed for intermediate triaxiality factors. The reason is probably the inability of the VgSCe to account for the localization of the strain field into bands which occurs inside the porous material as shown by Bilger et al. (2005). The large strain heterogeneity induced by the strain localization cannot efficiently be taken into account by the VgSCe since this latter does not allow for the ortho-radial heterogeneity of the secant modulus as explained in Section 2.3.

These first comparisons between the VgSCe and FFT simulations have been carried out for a particular class of microstructure for which the minimal distance separating the void edges is rather large (about 6 times the pore radius) and only for one realization of this microstructure. We now address more realistic situations for which this minimal distance is smaller and we consider six cherry-pit microstructures which correspond to six different minimal distances: 0.02, 0.04, 0.06, 0.08, 0.12 and 0.18 times the cell size W, while the pore radius is $0.033W$. For each distance, 10 statistical realizations are generated in order to balance the small size of the RVE – due to computer limitations, only 39 voids are included in the unit cell. The evolution of the effective yield stress under hydrostatic load derived from the VgSCe and from the FFT simulations as a function of the minimal distance is depicted in Fig. 13. The error bars refer to the extreme values of the computed stress among the 10 statistical realizations whereas the solid or dashed lines correspond to their averages. First, it is noted that the hydrostatic yield stress derived from the FFT simulations does not depend on the minimal distance for $d \leqslant 0.06W$. For larger d values, the yield stress increases with d, but remains significantly below the Gurson prediction. Both VgSCe's associated with either the Voronoï porosity distribution or the Stienen one fail to capture such an evolution. The former leads to a nearly constant yield stress slightly below or above the Gurson bound depending on whether d is smaller or larger than approximatively $0.09W$, respectively. In contrast to FFT simulations, the VgSCe derived from the Stienen porosity distribution is decreasing for increasing values of d. As expected, for large enough values of d, the hydrostatic yield stress is weaker than the Gurson one. However, for $d < d_0 \simeq 0.11W$, the VgSCe leads to a poor estimation of the hydrostatic yield stress and is stiffer than the Gurson bound. This is explained by the fact that the concentration c_0^S of the additional pattern representing the remaining matrix outside the composite inclusions becomes very large for small values of d: for instance $c_0^S \geqslant 85\%$ for $d \leqslant 0.08W$. This leads to a globally poor description of the nonlinear matrix behavior, as explained at the end of Section 3.3 for the simpler case with two pattern. Thus, when the voids are allowed to form clusters, *i.e.*, for small values of d, the VgSCe is unable to provide a good estimate of the yield surface for large triaxiality ratios. However, for a heterogeneous porosity distribution precluding the formation of clusters (large values of d), predictions of the VgSCe associated with the Stienen porosity distribution are in good agreement with the

results of the FFT simulations. At last, it is worth noting that the VgSCe is not restricted to periodic microstructures and that its computational cost is very low relative to that of FFT simulations.

5. Conclusion

A new micro-mechanical approach which incorporates local porosity fluctuations inside porous materials has been developed. This method leads to new rigorous bounds and estimates for the effective yield surface of porous media with a rigid-perfectly plastic matrix and a microstructure described by a generalized Hashin CSA, which may have the usual fractal structure, but does not necessarily so. In particular, new Hashin–Shtrikman-type upper bounds have been obtained. When applied to a classical (and not generalized) Hashin CSA – describing porous materials with a homogeneous distribution of pores, the obtained result, $\mathrm{VgHSb}_{\mathrm{hom}}$, improves on all earlier available bounds for this class of microstructures at all triaxiality ratios, and in particular on the sharp analytical Gărăjeu–Suquet upper bound.

When applied to the generalized Hashin CSA, with local porosity fluctuations, the main results derived from the proposed approach can be summarized as follows. First, the Hashin–Shtrikman-type upper bound, $\mathrm{VgHSb}_{\mathrm{het}}$, turns out to be very close to $\mathrm{VgHSb}_{\mathrm{hom}}$ even if slightly stiffer. The practical pertinence of the $\mathrm{VgHSb}_{\mathrm{het}}$ bound to assess the influence of a nonuniform distribution of voids on the effective plastic properties is however questionable since interactions between patterns are limited within this model. That is why self-consistent estimates such as the VgSCe estimate derived from the presented treatment are preferred.

Second, when the proportion of the additional pattern representing the remaining matrix outside the composite inclusions is not too large (typically less than about 85% for a global porosity of 10%), the VgSCe predicts a noticeable softening effect of local porosity fluctuations. Indeed, as shown in Section 3, the VgSCe is able to capture a sharper fall of the yield stress than that observed for the Gurson bound for high triaxiality factors. The softening of the yield stress under hydrostatic load due to porosity fluctuations can be explained by possible strain localization through soft zones near pores close to each other, described by patterns with a large local porosity: the easier the localization, depending on the microstructure and the associated pore connectedness, the lower the overall yield stress. The predicted strength drop is close to the difference between the heuristic Gurson–Tvergaard model and the Gurson bound, but is fully predictive since no fitting parameter is in principle required. However, for a very large proportion of the matrix only-made pattern, the VgSCe predictions are stiffer than Gurson estimates and tend to the classical self-consistent predictions even if always softer than these. This behavior is essentially due to the preponderance of the matrix only-made pattern inside which the heterogeneous plastic flow cannot be described accurately. This effect limits the domain of accuracy of the proposed approach to moderate and intermediate porosity fluctuations.

Third, comparisons between the VgSCe predictions and FFT simulations have been performed for the same simulated microstructures incorporating porosity fluctuations. They confirm the efficiency of the VgSCe associated with the Stienen scheme as long as the local porosity is not too heterogeneous. However, when voids are allowed to get into close contact and tend to form clusters, the VgSCe does not provide satisfactory results anymore since, as already explained, the proportion of the matrix outside the patterns is much too large.

Improvements of the proposed model can be expected from a modified pattern-based description of the microstructure, in which the proportion of the matrix-only pattern would be reduced, since, as mentioned in Section 2.2.3, the Stienen model is not optimal with respect to this criteria. In addition, the present treatment could in principle be extended to more general situations in which the voids and their distribution inside the matrix would be ellipsoidal. However, since no closed-form solutions are available for the associated auxiliary problem composed of a multilayer composite ellipsoidal inclusion embedded in the reference medium, finite element calculations similar to those used by Bornert (1996a) or other numerical tools would be required. Such a treatment would also allow to address more appropriately the gradient of the plastic flow along the orthoradial direction and permit the use of more complex patterns, such that the proportion of the matrix outside them could be reduced. Corresponding analyses are left for further investigations.

Acknowledgements

This study has benefited from the financial support of the Research and Development Division of Électricité de France. The authors wish to thank Renaud Masson and Gilles Rousselier for fruitful discussions about this subject.

Appendix A. Yield surfaces of porous materials

Expressions of the various available estimates or bounds for the yield surface of porous material which have been used in this paper for comparison purposes are recalled below.

Gurson criterion (Gurson, 1977)

$$\left(\frac{\Sigma_{\rm eq}}{\sigma_0}\right)^2 + 2f\cosh\left(\frac{3}{2}\frac{\Sigma_m}{\sigma_0}\right) - 1 - f^2 = 0. \tag{42}$$

Gurson–Tvergaard estimate (Tvergaard, 1981)

$$\left(\frac{\Sigma_{\rm eq}}{\sigma_0}\right)^2 + 2q_1 f\cosh\left(\frac{3}{2}q_2\frac{\Sigma_m}{\sigma_0}\right) - 1 - q_3 f^2 = 0. \tag{43}$$

From finite element simulations, Tvergaard has shown that using the values $q_1 \in [1.25; 2]$, $q_2 = 1$, $q_3 = q_1^2$ gives a reasonably accurate criterion for ductile porous solids.

Hashin–Shtrikman upper bound (Michel and Suquet, 1992)

$$\left(1 + \frac{2}{3}f\right)\left(\frac{\Sigma_{\rm eq}}{\sigma_0}\right)^2 + \frac{9}{4}f\left(\frac{\Sigma_m}{\sigma_0}\right)^2 - (1-f)^2 = 0. \tag{44}$$

Gărăjeu–Suquet upper bound (Gărăjeu and Suquet, 1997)

$$\tau(f)\left(\frac{\Sigma_{\rm eq}}{\sigma_0}\right)^2 + 2f\cosh\left(\frac{3}{2}\frac{\Sigma_m}{\sigma_0}\right) - 1 - f^2 = 0, \tag{45}$$

with

$$\tau(f) = \frac{1-f}{1 - 5f(16+19f^{7/3})/((3+2f)(16+19f^{7/3}) + 168f(1-f^{2/3})^2)}. \tag{46}$$

Gurson-HS estimate (Gărăjeu and Suquet, 1997) The Gurson-HS estimate is directly derived from the Gărăjeu–Suquet upper bound by replacing the definition of $\tau(f)$ in Eq. (46) by $\tau(f) = 1 + \frac{2}{3}f$

$$\left(1 + \frac{2}{3}f\right)\left(\frac{\Sigma_{\rm eq}}{\sigma_0}\right)^2 + 2f\cosh\left(\frac{3}{2}\frac{\Sigma_m}{\sigma_0}\right) - 1 - f^2 = 0. \tag{47}$$

References

Bardella, L., 2003. An extension of the secant method for the homogenization of the nonlinear behavior of composite materials. Int. J. Engrg. Sci. 41, 741–768.

Berveiller, M., Zaoui, A., 1979. An extension of the self-consistent scheme to plastically-flowing polycrystals. J. Mech. Phys. Solids 26, 325–344.

Bilger, N., Auslender, F., Bornert, M., Masson, R., 2002. New bounds and estimates for porous media with rigid perfectly plastic matrix. C. R. Mecanique 330, 127–132.

Bilger, N., Auslender, F., Bornert, M., Michel, J.-C., Moulinec, H., Suquet, P., Zaoui, A., 2005. Effect of nonuniform distribution of voids on the plastic response of voided materials: a computational and statistical analysis. Int. J. Solids Structures 42, 517–538.

Bornert, M., 1996a. A generalized pattern-based self consistent scheme. Comp. Mat. Sci. 5, 17–31.

Bornert, M., 1996b. Morphological effects at the local scale in two-phase materials. In: Pineau, A., Zaoui, A. (Eds.), Micromechanics of Plasticity and Damage of Multiphase Materials. Kluwer Academic Publishers, pp. 27–34.

Bornert, M., 2001. Homogénéisation des milieux aléatoires, bornes et estimations. Hermes Science (Chapter 5, pp. 133–221).

Bornert, M., Hervé, E., Stolz, C., Zaoui, A., 1994. Self-consistent approaches and strain heterogeneities in two-phase elastoplastic materials. Appl. Mech. Rev. 47, 66–76.

Bornert, M., Stolz, C., Zaoui, A., 1996. Morphologically representative pattern-based bounding in elasticity. J. Mech. Phys. Solids 44, 307–331.

Christensen, R.M., Lo, K.H., 1979. Solution for effective shear properties in three phase sphere and cylinder models. J. Mech. Phys. Solids 27, 315–330.

Coster, M., Chermant, J., 2002. On a way to material models for ceramics. J. Eur. Ceram. Soc. 22, 1191–1203.

Gărăjeu, M., Suquet, P., 1997. Effective properties of porous ideally plastic or viscoplastic materials containing rigid particles. J. Mech. Phys. Solids 45, 873–902.

Gurson, A., 1977. Continuum theory of ductile rupture by void nucleation and growth: Part I. Yield criteria and flow rules for porous ductile media. J. Eng. Mat. Tech 99, 1–15.

Hashin, Z., 1962. The elastic moduli of heterogeneous materials. J. Appl. Mech., 143–150.
Hashin, Z., Shtrikman, S., 1963. A variational approach to the theory of the elastic behavior of multiphase materials. J. Mech. Phys. Solids 11, 127–140.
Hervé, E., Stolz, C., Zaoui, A., 1991. A propos de l'assemblage de sphères composites de Hashin. C. R. Acad. Sci. Paris 313, 857–862.
Hervé, E., Zaoui, A., 1993. N-layered inclusion-based micromechanical modelling. Int. J. Engrg. Sci. 31 (1), 1–10.
Hill, R., 1965. Continuum micro-mechanics of elastoplastic polycrystals. J. Mech. Phys. Solids 13, 89–101.
Hutchinson, J.W., 1970. Elastic-plastic behaviour of polycrystalline metals and composites. Proc. R. Soc. London Ser. A 319, 247–272.
Kailasam, M., Ponte Castañeda, P., Willis, J.R., 1997. The effect of particle size, shape, distribution and their evolution on the constitutive response of nonlinearly viscous composites. II. Examples. Philos. Trans. R. Soc. London Ser. A 355, 1853–1872.
Koplik, J., Needleman, A., 1988. Void growth and coalescence in porous plastic solids. Int. J. Solids Structures 24, 835–853.
Kreher, W., 1990. Residual stresses and stored elastic energy of composites and polycrystals. J. Mech. Phys. Solids 38 (1), 115–128.
Masson, R., Bornert, M., Suquet, P., Zaoui, A., 2000. An affine formulation for the prediction of the effective properties of nonlinear composites and polycrystals. J. Mech. Phys. Solids 48, 1203–1227.
Michel, J.-C., Moulinec, H., Suquet, P., 1999. Effective properties of composites materials with periodic microstructure: a computational approach. Comput. Methods Appl. Mech. Engrg. 172, 109–143.
Michel, J.-C., Moulinec, H., Suquet, P., 2000. A computational method based on augmented lagrangians and fast Fourier transforms for composites with high contrast. Comput. Modelling Engrg. Sci. 1 (2), 79–88.
Michel, J.-C., Suquet, P., 1992. The constitutive law of nonlinear viscous and porous materials. J. Mech. Phys. Solids 40 (4), 783–812.
Molinari, A., Canova, G., Ahzi, S., 1987. A self-consistent approach of the large deformation polycrystal viscoplasticity. Acta Metall. 35 (12), 2983–2994.
Moulinec, H., Suquet, P., 1994. A fast numerical method for computing the linear and the nonlinear mechanical properties of composites. C. R. Acad. Sci. Paris Ser. II 318, 1417–1423.
Moulinec, H., Suquet, P., 1998. A numerical method for computing the overall response of nonlinear composites with complex microstructure. Comput. Methods Appl. Mech. Engrg. 157, 69–94.
Perrin, G., 1992. Contribution à l'étude théorique et numérique de la rupture ductile des métaux. Ph.D. thesis, Ecole Polytechnique, France.
Perrin, G., Leblond, J., 1990. Analytical study of a hollow sphere made of plastic porous material and subjected to hydrostatic tension – Application to some problems in ductile fracture of metals. Int. J. Plasticity 6, 677–699.
Pijnenburg, K., Van der Giessen, E., 2001. Macroscopic yield in cavitated polymer blends. Int. J. Solids Structures 38, 3575–3598.
Ponte Castañeda, P., 1991. The effective mechanical properties of nonlinear composites. J. Mech. Phys. Solids 39, 45–71.
Ponte Castañeda, P., 1992. New variational principles in plasticity and their application to composite materials. J. Mech. Phys. Solids 40 (8), 1757–1788.
Ponte Castañeda, P., 1996. Exact second-order estimates for the effective mechanical properties of nonlinear composite materials. J. Mech. Phys. Solids 44, 827–862.
Ponte Castañeda, P., 2002. Second-order homogenization estimates for nonlinear composites incorporating field fluctuations: I – Theory. J. Mech. Phys. Solids 50, 737–757.
Ponte Castañeda, P., Willis, J.R., 1995. The effect of spatial distribution on the effective behavior of composite materials and cracked media. J. Mech. Phys. Solids 43 (12), 1919–1951.
Richelsen, A.B., Tvergaard, V., 1994. Dilatant plasticity for upper bound estimates for porous ductile solids. Acta Metall. Mater. 42 (8), 2561–2577.
Salençon, J., 1983. Calcul à la rupture et analyse limite. Presses de l'ENPC.
Stolz, C., Zaoui, A., 1991. Analyse morphologique et approches variationnelles du comportement d'un milieu élastique hétérogène. C. R. Acad. Sci. Paris Ser. II 312, 143–150.
Suquet, P., 1983. Analyse limite et homogénéisation. C.R. Acad. Sci. Paris Ser. II 296, 1355–1358.
Suquet, P., 1995. Overall properties of nonlinear composites: a modified secant moduli theory and its link with Ponte Castañeda's nonlinear variational procedure. C. R. Acad. Sci. Paris Ser. II 320, 563–571.
Suquet, P., 2005. On the effet of small fluctuations in the volume fraction of constituents on the effective properties of composites. C. R. Mecanique 333, 219–226.
Torquato, S., 2003. Random Heterogeneous Materials. Springer-Verlag, Berlin.
Trillat, M., Pastor, J., 2005. Limit analysis and Gurson's model. Eur. J. Mech. A Solids 24, 800–819.
Tvergaard, V., 1981. Influence of void on shear band instabilities under plane strain conditions. Int. J. Frac. 17, 389–407.
Tvergaard, V., 1990. Material failure by void growth to coalescence. In: Hutchinson, J., Wu, T. (Eds.), Advances in Applied Mechanics, vol. 27. Academic Press, New York, pp. 83–151.
Tvergaard, V., Needleman, A., 1984. Analysis of the cup-cone fracture in a round tensile bar. Acta Metall. Mater. 32, 157–169.
Willis, J., 1991. On methods for bounding the overall properties of nonlinear composites. J. Mech. Phys. Solids 39, 73–86.